A spectral anelastic Navier–Stokes solver for a stratified two-miscible-layer system in infinite horizontal channel

Nicolas Schneider, Zohra Hammouch, Gérard Labrosse, Serge Gauthier

A spectral anelastic Navier–Stokes solver for a stratified two-miscible-layer system in infinite horizontal channel

Nicolas Schneider [a], Zohra Hammouch [a,1], Gérard Labrosse [b,2], Serge Gauthier [a,*]

[a] CEA, DAM, DIF, Bruyères-le-Châtel, F-91297 Arpajon, France
[b] Université Paris-Sud 11, Département de Physique, 91405 Orsay Cedex, France

We present a consistent Chebyshev–Fourier–Fourier pseudo-spectral algorithm for the numerical solution of anelastic models. These models satisfy the constraint $\partial_i(\widetilde{\rho}\, u_i) = 0$, where $\widetilde{\rho}$ is a mean density profile and u the velocity field. The choice of the decoupling method is discussed and the Uzawa approach is generalized to such a constraint. The pressure operator properties are detailed and the solution of the zeroth Fourier mode case is discussed. The solution of linear systems is obtained and refined, using an iterative method. The Uzawa algorithm is embedded in an auto-adaptive multidomain approach in order to handle steep evolving gradients. The algorithm is reduced to the Boussinesq approximation. The characteristics and performance of the resulting numerical code are analyzed. The validation includes comparisons with linear stability results and with the Waddell et al. [55] single-mode experiment. We also compute the nonlinear growth rate of a Boussinesq turbulent mixing layer. A comparison between Boussinesq and anelastic models is then sketched out. Finally four 3D simulations are carried out (with the anelastic and Boussinesq models). These results illustrate the capability of the entire method to handle stiff problems such as the Rayleigh–Taylor configuration.

1. Introduction

This paper presents a consistent Chebyshev–Fourier–Fourier pseudo-spectral algorithm for solving anelastic approximations of the Navier–Stokes equations. The continuity constraint is expressed by $\partial_i\,(\widetilde{\rho}(z)\,u_i) = 0$, instead of the more classical constraint $\partial_i u_i = 0$ of the Boussinesq approximations. The velocity field is u and $\widetilde{\rho}(z)$ is a mean density profile. Such approximations appear in various domains, for example in the anelastic model for thermal convection [3,4,19,26,41,44] or the recently built anelastic approximation for Rayleigh–Taylor (RT) flows [29,51].

The coupling between the velocity and the pressure leads to a significant computational difficulty. This numerical complication already occurs in the Boussinesq case, but is appreciably more important in the anelastic configuration. Indeed, in the Boussinesq case, there are many ways to decouple the velocity from the pressure. They can be organized into four families, which are listed in Table 1 along with their main qualities and limitations. One of these families, the 'time splitting', is efficient in computational time but inconsistent with the continuous formulation of the decoupling [32,36]. However this option was adopted by Barranco and Marcus [4] in their analysis, which is based on a spectral solver of the Navier–Stokes

* Corresponding author.
E-mail address: Serge.Gauthier@orange.fr (S. Gauthier).
[1] Present address: C-S, 22 avenue Galilée, F-92350 Le Plessis Robinson.
[2] Retired.

Table 1
Boussinesq–Stokes pseudo-spectral solver families. Column 4 states whether or not the scheme uses the relation $\partial_i u_i = 0$ as a constitutive equation (yes) or as a constraint (no).

Decoupling option	Consistency	Computational cost	$\partial_i u_i \stackrel{?}{=} 0$
Uzawa [2]	yes	expensive	yes
Green or influence matrix [33]	yes	expensive	yes
Time splitting [14,53]	no	low	no
Projection-Diffusion [5]	yes	low	no

Table 2
Numerical contributions to the RTI investigation restricted to low Mach number and Boussinesq approximations (DNS: Direct Numerical Simulation, LES: Large Eddy Simulation).

Physical model	DNS	LES
Incompressible Euler ($\partial_i u_i = 0$)	Joly et al. [31]	
Boussinesq Navier–Stokes ($\partial_i u_i = 0$)	Young et al. [56] Ristorcelli and Clark [49] Vladimirova and Chertkov [54] Boffetta et al. [8]	
Sandoval model [50] ($\partial_i u_i \neq 0$)	Cook and Dimotakis [16] Cabot and Cook [11] Livescu and Ristorcelli [38] Mueschke and Schilling [42,43] Zhang and Tan [58] Livescu et al. [39]	Cook et al. [17] Cabot [10]
Low Mach number Euler		Bell et al. [7] Zingale et al. [59]
Anelastic ($\partial_i \widetilde{\rho} u_i = 0$)	this work	

equations. The optimal decoupling approach is the Projection-Diffusion method, even taking into account the fact that the numerical divergence does not vanish at the space nodes but exponentially decays with the node number. This can be expected from a simple argument. Assuming that the exact velocity field is known, its numerical divergence will never vanish except asymptotically when the grid refinement becomes infinite. Consequently, imposing $\partial_i u_i = 0$ at all the nodes results in adding some numerical errors to the velocity field. Since the Projection-Diffusion method does not seem to be generalizable to the anelastic approximation, the present numerical option is based on the Uzawa decoupling method. Table 1 declares this method as expensive in computational time. This is the case for 2D/3D confined flows. In the present work, the horizontal periodicity of the flow suppresses this limitation, while requiring an important memory space for storing the Uzawa operator for each horizontal wave number.

On the other hand the Rayleigh–Taylor instability (RTI) is one of the numerous hydrodynamic instabilities that has many scientific, industrial and natural applications. The analysis of its evolution with time until the last turbulent mixing stage is always of interest and it deserves accurate and well-adapted numerical tools. This instability can be tackled in various physical configurations, for example with miscible or immiscible fluid layers, with compressible or incompressible flows, viscous or inviscid fluids, or, finally, triggered by large- or small-scale initial conditions. For a review, see [1] and references therein, for some visualizations, see [52]. This instability occurs at the interface between two miscible fluid layers, the heavier layer being stacked on top of the lighter one. Both layers are stably stratified in the presence of an acceleration field.

This situation has been analyzed with a large variety of numerical tools as indicated in Table 2, which gathers most of the published contributions to this topic. Many contributions have also been made in the fully compressible regime using either Euler or Navier–Stokes equations [22,24,37]. The compressible option contains the three Kovásznay modes, [15], i.e., the vorticity, entropic and acoustic modes. The low-Mach number approximations contain the vorticity mode and a degraded entropic mode while the Boussinesq one contains only the vorticity mode. It should be noted that the word 'compressible' is often used with two different meanings. The first meaning is used in the case of static compressibility, in which an acceleration field generates a density stratification with its length scales, $\left|L_{\rho_H}\right|$ and $\left|L_{\rho_L}\right|$ for the heavy and light fluids respectively, L_{ρ_H} with $L_{\rho_{H,L}}^{-1} = (1/\rho_{H,L})\,(d\rho_{H,L}/dz)$. The second meaning corresponds to the 'dynamic compressibility' case. It is mainly associated with the acoustic dynamics or the equation of state. For a perfect gas, this effect is governed by the adiabatic indexes of the two fluids, γ_H and γ_L. A practical consequence of the presence of acoustic waves is to dramatically lower the time step in numerical simulations. This is the main reason why an approximation where the 'dynamic compressibility' can be discarded is interesting if the acoustic contribution to the flow is not important. In a recent study by Schneider and Gauthier [51] an asymptotic analysis—carried out in terms of the small parameter $\gamma\, Ma^2 \ll 1$, Ma being the flow Mach number—has been used to derive the anelastic, the quasi-isobaric and the Boussinesq approximations of the RT flow. In particular, the anelastic approximation keeps the 'static compressibility' into play and appears to remain valid for slightly stratified equilibrium states. The anelastic configuration contains the vorticity and entropic modes, the acoustic

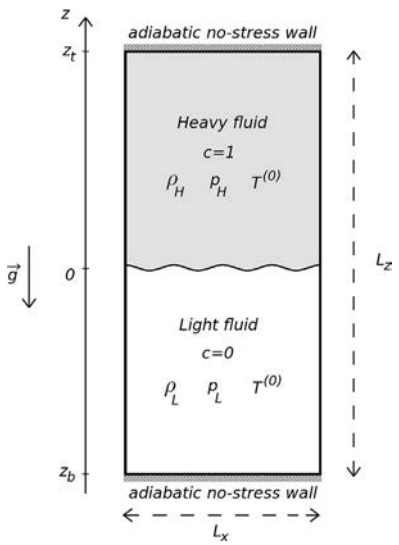

Fig. 1. Sketch of the RT initial configuration: a heavy fluid layer is stably stratified and stacked on top of a light one, stably stratified also, in presence of an acceleration field, $\vec{g}$.

mode being filtered out by the model. As can be seen in Table 2, so far this configuration has not received as much attention as the others have. This is surprising since the stratification of both layers has an important effect on the evolution of the instability, even when neglecting the acoustic contribution. The goal is therefore to achieve a physically reliable analysis of this configuration of the RTI and of its capability to generate, in time, small length scales until turbulence is fully developed.

This paper presents a generalization of the consistent Uzawa decoupling method to the anelastic model within the framework of spectral methods. Properties of this numerical scheme are detailed: condition number of the main operator, accuracy and performance. Spectral accuracy is achieved. This algorithm is coupled with an auto-adaptive Chebyshev multidomain method, which is shown to be capable of handling stiff problems such as the RTI. The entire method and the numerical code are validated against linear stability results, and single- and multi-mode RT-experiments.

Section 2 is devoted to the description of the anelastic and Boussinesq models. Section 3 is dedicated to the presentation of the numerical algorithms. In particular, the Uzawa uncoupling method for the anelastic approximation of the Navier–Stokes problem is detailed. Section 4 studies spatial and temporal convergence and the optimal multidomain grid. It also gives some computational features of the resulting numerical code. Section 5 is dedicated to validation. Finally in Section 6 the capability of the entire method is illustrated with some physical examples and with a comparison between Boussinesq and anelastic models.

2. Anelastic and Boussinesq models

2.1. Anelastic model

In this section, we present the governing equations and the mixing model. The initial and final profiles of the thermodynamic variables are also given. The motion takes place in a three-dimensional horizontal channel (L_x, L_y, L_z) where $L_z = z_t - z_b$ and the volume is $V = L_x L_y L_z$ (see Fig. 1). The coordinates z_b and z_t are the bottom and top of the domain respectively. The heavy fluid (subscript H) is initially located in the upper side of the domain, i.e., for $0 \leq z \leq z_t$, on top of a light fluid (subscript L) occupying the region $z_b \leq z \leq 0$. The mixing of these two miscible fluids is analyzed within the framework of the single fluid approximation where the partial densities are $\overline{\rho}_H^{xyz} = m_H/V$ and $\overline{\rho}_L^{xyz} = m_L/V$. The operator $\overline{\ }^{xyz}$ stands for the average value over the three-directions (x, y, z) and $m_{H,L}$ are the masses of the heavy and light fluids contained in the volume V. We use the 'partial pressures–partial densities' mixing model such as

$$p = p_H + p_L \quad \text{and} \quad \rho = \rho_H + \rho_L. \tag{1}$$

The expression of the partial pressures reads

$$p_i = \rho_i \frac{\mathcal{R}}{\mathcal{M}_i} T = (\gamma_i - 1)\rho_i C_{v_i} T, \quad \text{with} \quad i = H, L, \tag{2}$$

where $\mathcal{R}$ is the perfect-gas constant and $\mathcal{M}_{H,L}$ are the molar weights. The specific heats at constant volume are C_{v_i} and γ_i are the isentropic indexes. We also define a fluid concentration c,

$$\rho_H = c\,\rho \quad \text{and} \quad \rho_L = (1 - c)\,\rho. \tag{3}$$

According to the additivity of the extensive variables, the specific heats C_{v_i}'s and indexes γ_i's of the mixing depend on the concentration c. The system of equations is adimensionalized with the following four reference quantities *(i)* length: $L_r = L_y$, *(ii)* time: $t_r = \left(L_y/g\right)^{1/2}$, where g is the acceleration due to gravity, *(iii)* density: $\rho_r = \left(\rho_H(0^+) + \rho_L(0^-)\right)/2$, *(iv)* temperature: $T_r = T^{(0)}$, the uniform temperature of the equilibrium state. The pressure of reference is $p_r = \rho_r\,(\mathcal{R}/\mathcal{M}_r)\,T_r$ with $2/\mathcal{M}_r = 1/\mathcal{M}_H + 1/\mathcal{M}_L$. The concentration of reference is chosen to be $c_r = (1 - At)/2$, where At is the Atwood number defined below, and the reference value for the specific heat ratio of the mixing is $\gamma_r = \gamma(c_r)$. Finally the reference specific heat is defined as $C_{v,r} = (\gamma_r - 1)^{-1}\mathcal{R}/\mathcal{M}_r$. The expression of the dimensionless numbers, Atwood, Reynolds, stratification Sr, Schmidt and Prandtl, expressed within the reference scales are

$$
\begin{aligned}
&At = \frac{\rho_H(z=0^+,t=0) - \rho_L(z=0^-,t=0)}{\rho_H(z=0^+,t=0) + \rho_L(z=0^-,t=0)},\\
&Re = \frac{g^{1/2}\,L_r^{3/2}}{\mu/\rho_r},\ Sr = \frac{g\,L_r}{\mathcal{R}\,T_r/\mathcal{M}_r},\ Sc = \frac{\mu}{\rho_r\,\mathcal{D}} \quad \text{and} \quad Pr = \gamma_r\,\frac{\mu\,C_{v,r}}{\kappa}.
\end{aligned}
\tag{4}
$$

Anelastic approximations use the general form of the continuity equation [13]

$$
\partial_i(\widetilde{\rho}(z)\,u_i) = 0, \tag{5}
$$

where $\widetilde{\rho}$ is some characteristic density and u_i is the ith-velocity component. For RT configurations, various density profiles may be considered. During the development of an RT-mixing layer, the mean density profile starts with a sharp discontinuity. This density jump decreases with time. At the end of the mixing process, the density profile is one-dimensional and given by the hydrostatic equilibrium of the homogeneous mixing. In a recent paper devoted to incompressible type models for RT-flows [51], we have used this one-dimensional final state density profile as the characteristic density (5) to build an anelastic approximation for RT-flows. Within this framework, thermodynamic variables are split into zeroth and first-order quantities. The zeroth order corresponds to the final equilibrium state, the first order is the fluctuations supposed to be much smaller than the zeroth order. We write

$$
\begin{aligned}
&\rho = \rho^{(0)} + \rho^{(1)}, \qquad c = c^{(0)} + c^{(1)}, \qquad p = p^{(0)} + p^{(1)},\\
&T = T^{(0)} + T^{(1)}, \qquad e = e^{(0)} + e^{(1)},
\end{aligned}
\tag{6}
$$

where T and e are the temperature and internal energy, respectively. The velocity is of zeroth order and is denoted u_i. One then obtains the following set of adimensionalized equations

$$
\rho^{(0)}(\partial_t u_i + u_j\,\partial_j u_i) = -\frac{1}{Sr}\,\partial_i p^{(1)} + \frac{1}{Re}\,\partial_j\sigma_{ij} - \rho^{(1)}\,\delta_{i3}, \tag{7}
$$

with the constraint $\partial_i\,(\rho^{(0)}\,u_i) = 0$. The internal energy equation is

$$
\begin{aligned}
\partial_t\rho^{(0)}\,e^{(1)} + \partial_i\rho^{(0)}\,u_i\,e^{(1)} = &-(\gamma_r - 1)\,p^{(1)}\,\partial_i u_i + (\gamma_r - 1)\,\frac{Sr}{Re}\,\sigma_{ij}\,D_{ij}\\
&+ \frac{\Delta_{H,L}}{Sc\,Re}\,\partial_i[T^{(0)}\,(\rho^{(0)}\,\mathcal{D}^\star)\,\partial_i c^{(1)}] + \frac{\gamma_r}{Pr\,Re}\,\partial_i(\kappa^\star\,\partial_i T^{(1)}),
\end{aligned}
\tag{8}
$$

and the advection–diffusion equation for the concentration is

$$
\rho^{(0)}(\partial_t c + u_j\,\partial_j c) = \frac{1}{Sc\,Re}\,\partial_i(\rho^{(0)}\,\mathcal{D}^\star\,\partial_i c). \tag{9}
$$

The previous system is closed with the linearized form of the perfect gas EOS

$$
\frac{p^{(1)}}{p^{(0)}} = \frac{\rho^{(1)}}{\rho^{(0)}} + \frac{T^{(1)}}{T^{(0)}} - \frac{2\,At\,c^{(1)}}{1 + At - 2\,At\,c^{(0)}}. \tag{10}
$$

Zeroth-order quantities (with the superscript (0)) only depend on the vertical coordinate z. The partial derivative with respect to x_i is denoted ∂_i. The viscous stress tensor $\sigma_{ij} = \mu^\star(\partial_j u_i + \partial_i u_j - 2/3\,\delta_{ij}\partial_\ell u_\ell)$ is defined within the Stokes approximation. D_{ij} is the rate-of-deformation tensor. The difference of specific heats at constant pressure of the two species is $\Delta_{H,L} = (C_{p\,H} - C_{p\,L})/C_{v,r}$, where $C_{v,r}$ is the reference value. The transport coefficients $\mu^\star$, $\kappa^\star$ and $\mathcal{D}^\star$ are taken as constants equal to 1. In the following, we will use indifferently either (x, y, z) or x_i for the coordinates. The boundary conditions are periodic in the horizontal (x, y)-directions for all physical quantities. Indeed, RT-studies are often motivated by astrophysics or inertial confinement fusion where flows develop in spherical geometry. We thus approximate these flows in rectangular domains with horizontal periodic boundary conditions. There is no flow and therefore no mass flux through the top and bottom channel walls. Moreover there is no stress along the walls. We also impose a zero heat flux through the channel walls. Consequently the boundary conditions are

$$
\begin{aligned}
&\partial_z u_{1,2}\big|_{x,z=z_b,z_t;t} = u_3(x, z=z_b, z_t; t) = 0,\\
&\partial_z T^{(1)}\Big|_{x,z=z_b,z_t;t} = \partial_z c|_{x,z=z_b,z_t;t} = 0.
\end{aligned}
\tag{11}
$$

Appropriate initial conditions have to be added. Equations (7)–(11) are restricted to $Sr \neq 0$ and $At \neq 1$. They are considered as a good approximation when the stratification Sr is of the order of 1. Indeed for large values of Sr the dynamic compressibility plays a significant role. The linear part of (7) with the constraint $\partial_i(\rho^{(0)}(z)\,u_i) = 0$, i.e., the anelastic Stokes problem, is shown to be elliptic [30].

The section ends with two remarks, useful for the numerical approach detailed below [51]. First mass conservation is not guaranteed with the system of equations (7)–(11). It has to be imposed explicitly, $\int \rho^{(1)}\,dV = 0$. This conservation law is derived from the continuity equation of the full Navier–Stokes equations. Second the dynamic equation (7) is invariant under the transformation $p^{(1)} \to p^{(1)} + \alpha_p\,p^{(0)}$, where α_p is an arbitrary constant [3,44]. Indeed the density fluctuations appearing in equation (7) may be expressed with the EOS (10). In this way, the operator $Sr^{-1}\partial_z - \rho^{(0)}/p^{(0)}$ applies on the dynamic pressure $p^{(1)}$ and the above invariance may be checked. The correct level of dynamic pressure fluctuations $p^{(1)}$ is imposed through mass conservation, which turns out to be an equation for the constant α_p. The entire system (6)–(10) is not invariant under this transformation.

2.2. Initial equilibrium state

The hydrostatic equilibrium in both the heavy and the light fluids with a uniform temperature $T^{(\mathrm{ini})}$ provides the initial one-dimensional steady state ($\rho^{(\mathrm{ini})}$, $u_i \equiv 0$, $T^{(\mathrm{ini})}$, $c^{(\mathrm{ini})}$ and $p^{(\mathrm{ini})}$). Using equation (7), hydrostatic balance becomes

$$Sr^{-1}\,d_z p_i^{(\mathrm{ini})} + \rho_i^{(\mathrm{ini})} = 0 \qquad \text{for} \quad i = H, L. \tag{12}$$

The total density profile is built with the regularized Heaviside functions $H_\pm(z) = (1 \pm \mathrm{erf}(z/\delta))/2$, where the parameter δ represents the width of the initial pseudo-interface thickness. The total density is expressed by

$$\rho(z) = (1 + At)\exp(-Sr_H\,z)H_+(z) + (1 - At)\exp(-Sr_L\,z)H_-(z), \tag{13}$$

where $Sr_{H,L} = Sr/(1 \mp At)$. The regularized concentration profile is obtained from $c^{(\mathrm{ini})}(z) = \rho_H^{(\mathrm{ini})}(z)/\rho^{(\mathrm{ini})}(z)$. The pressure is analytically calculated from Eq. (12) as $p^{(\mathrm{ini})}(z) = -Sr\int \rho^{(\mathrm{ini})}(z)\,dz$. The integration constant is adjusted in such a way that the boundary condition $T^{(\mathrm{ini})}(z_b) = 1$ is satisfied. Finally the temperature profile is recalculated from the EOS.

2.3. Final equilibrium state

After the overturn of the fluids, the flow tends asymptotically toward an equilibrium state, which only depends on the inhomogeneous z-coordinate. In this regime, the velocities fall to zero and the density reaches a non-uniform constant profile denoted $\rho^{(\mathrm{end})}(z)$. In the same way, equation (9) for the concentration c with Neumann boundary conditions shows that c reaches asymptotically a uniform and constant value denoted $c^{(\mathrm{end})}$. This value is simply given by the expression

$$c^{(\mathrm{end})} = \frac{m_H}{m_H + m_L}. \tag{14}$$

The density profile $\rho^{(\mathrm{end})}$ is obtained by considering the momentum equation

$$-Sr^{-1}(1 + At - 2\,At\,c^{(\mathrm{end})})\,d_z\rho^{(\mathrm{end})}(z) = \rho^{(\mathrm{end})}(z), \tag{15}$$

the solution of which is

$$\rho^{(\mathrm{end})}(z) = \rho^{(\mathrm{end})}(0)\,\exp(-\mathcal{S}\,z), \tag{16}$$

where $\mathcal{S} = Sr\,(1 + At - 2\,At\,c^{(\mathrm{end})})^{-1}$. The constant $\rho^{(\mathrm{end})}(0)$ is fixed with the total mass, $m_H + m_L$, of the two fluids

$$\rho^{(\mathrm{end})}(0) = \frac{(m_H + m_L)\,\mathcal{S}}{\exp(-\mathcal{S}\,z_b) - \exp(-\mathcal{S}\,z_t)}. \tag{17}$$

2.4. Boussinesq model

For small Atwood numbers and unstratified equilibrium states, the full Navier–Stokes equations reduce to the so-called Boussinesq approximation, which writes [51]

$$\partial_t u_i + u_j\,\partial_j u_i = -\partial_i p + Re^{-1}\,\partial^2_{jj} u_i - (2\,c - 1)\,\delta_{i3},$$

with the constraint $\partial_i u_i = 0$,

$$\partial_t c + u_j\,\partial_j c = (Sc\,Re)^{-1}\,\partial_{ii} c, \tag{18}$$

where p is defined up to an additive constant. System (18) involves only the vorticity mode; the entropic and acoustic modes have been removed. This system of PDEs is of elliptic type. The boundary conditions are the same as for the anelastic case (system (11)) but without considering the temperature. Appropriate initial conditions have to be added.

Two examples of density profiles are displayed in Fig. 2, one for a Boussinesq unstratified configuration at $At = 0.10$, one for an anelastic stratified configuration, with $At = 0.25$ and $Sr = 2$.

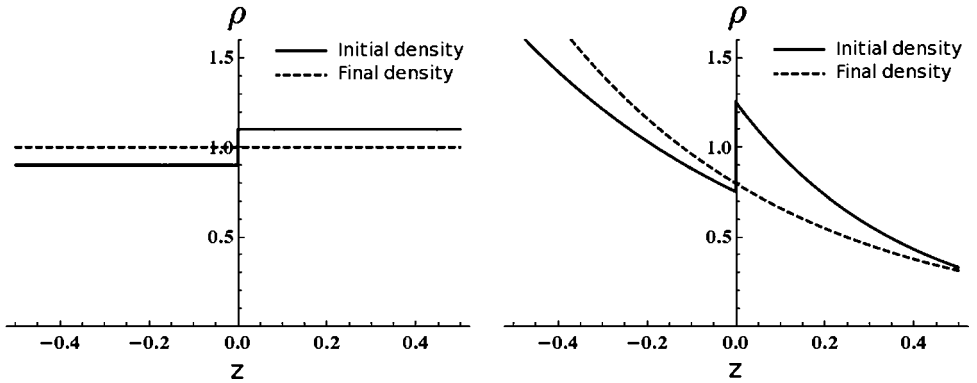

Fig. 2. Density profiles for the RTI. The full lines represent the initial unstable profiles and the dashed lines represent the stable density profiles after the overturn of the two fluids. Left: $At = 0.10$ Boussinesq unstratified configuration. Right: typical anelastic configuration with $At = 0.25, Sr = 2$; the heavy and light fluids are stably stratified although the stack is unstable.

3. Numerical algorithms

The problem to be solved is made of the Navier–Stokes, concentration and energy equations with an EOS, (7)–(11). Space discretization utilizes a non-overlapping Chebyshev multidomain method in the z-inhomogeneous direction. A coordinate transform is defined in each subdomain. A Fourier method is used in the (x, y)-homogeneous directions. Time marching is handled in the Fourier space, with a second-order three-step semi-implicit low-storage Runge–Kutta method ([12], Section 4.3.2). The velocity equation and the associated constraint lead to a generalized Stokes problem while the concentration and the energy equations lead to Helmholtz problems. Physical quantities $\phi = \rho$, u_i, p, T and c are first expanded on Fourier series along the (x, y)-directions:

$$\phi^{(m)}(x, y, z, t) = \sum_{k_x=-N_x/2}^{N_x/2-1} \sum_{k_y=-N_y/2}^{N_y/2-1} \widetilde{\phi}^{(m)}_{k_x k_y}(z, t)\, e^{\,\mathrm{i}\,(k_x x + k_y y)}, \tag{19}$$

with $m = 1, \ldots, M$, where M is the number of subdomains. The following change of variables is carried out on the horizontal velocity components $(\widetilde{u}_1, \widetilde{u}_2)$

$$\begin{aligned} k\,\widetilde{v}^{(m)}_k &= \mathrm{i}k_x\,\widetilde{u}^{(m)}_{1,k} + \mathrm{i}k_y\,\widetilde{u}^{(m)}_{2,k}, \\ k\,\widetilde{v}^{\perp\,(m)}_k &= \mathrm{i}k_x\,\widetilde{u}^{(m)}_{1,k} - \mathrm{i}k_y\,\widetilde{u}^{(m)}_{2,k}, \end{aligned} \tag{20}$$

where $k = \sqrt{k_x^2 + k_y^2}$, $k \geq 0$. The vertical velocity $w \equiv u_3$ and the pressure $p^{(1)}$ remain unchanged. This change of variables allows us to decouple the velocities $\widetilde{v}^{(m)}_k$ and $\widetilde{v}^{\perp\,(m)}_k$. The complex number i has been used in (20) in order to only deal with real operators. The variables $(\widetilde{v}, \widetilde{p})$ are solution of a generalized Stokes problem while the velocity $\widetilde{v}^{\perp}$, the concentration and the temperature are solution of Helmholtz problems. This Stokes problem is solved by means of both the Uzawa algorithm and the influence matrix method [40,47]. Continuity of the dependent variables and of their first derivatives is required for quantities governed by second-order PDEs, i.e., velocity, temperature and concentration. In the influence matrix method, the velocity unknowns are written as a linear combination of 5 elementary solutions, each one being solution of a Stokes problem with specific boundary conditions. The coefficients of these linear combinations are solution of a $2(M + 1)$-order linear system. A similar procedure is used to solve the Helmholtz equations with 3 elementary solutions and $M + 1$-order linear systems.

The matching conditions at the subdomain interfaces depend on the nature of the PDEs to be solved ([12], Chap. 13). It is quite natural to impose the continuity of the velocity. Then the continuity of the force at the interfaces provides more conditions. The stress tensor and the pressure generate a force on the elementary surface whose expression in the vertical direction is

$$df_i = (\sigma_{ij} - p\,\delta_{ij})\,n_j\,dS \qquad i, j = 1, 2, 3, \tag{21}$$

where n is the normal vector at the interface. For horizontal interfaces ($j = 3$), the expression of the force is

$$df_i = ((\partial_3 u_i + \partial_i u_3 - 2/3\,\delta_{i3}\,\partial_\ell u_\ell) - p\,\delta_{i3})\,dS, \qquad i = 1, 2, 3. \tag{22}$$

The continuity of the z-derivative of the velocity components and the continuity of the pressure follows the continuity of this force. Notice that the continuity of the second z-derivative of the vertical velocity, $\partial^2_{zz} w$, ensues from the constraint $\partial_i\,(\rho^{(0)}\,u_i) = 0$. Indeed, in the Fourier space, this constraint writes

$$k\widetilde{v}_k^{(m)} + \partial_z \widetilde{w}_k^{(m)} + L_\rho^{-1}\widetilde{w}_k^{(m)} = 0. \tag{23}$$

Considering the matching conditions derived above, the z-derivative of this equation leads to the result. It is worth noticing that there is no constraint on the continuity of the pressure derivative.

3.1. Anelastic Stokes problem

The Stokes problem describes the time and space evolution of the fluid velocity $u_i(x, y, z, t)$ and of the dynamic pressure $p^{(1)}(x, y, z, t)$. The uncoupling between the velocity and pressure is then worked out.

Consider the open domain Ω defined by $x, y \in (]-\infty, +\infty[)^2$ and $z \in \cup]z_a^{(m)}, z_b^{(m)}[$, and the domain $\overline{\Omega} = \cup [z_a^{(m)}, z_b^{(m)}]$, $m = 1, \ldots, M$, which is closed in z. We obviously have $z_a^{(1)} = z_b$ and $z_b^{(M)} = z_t$. Let u_i and $p^{(1)}$ be the solution of the following dimensionless problem,

$$\begin{aligned}\rho^{(0)}(\partial_t u_i + u_j\,\partial_j u_i) = &-\left(\frac{1}{Sr}\,\partial_i + \frac{\rho^{(0)}}{p^{(0)}}\delta_{i3}\right) p^{(1)} \\ &+ \frac{1}{Re}\left(\partial_{jj}u_i - \frac{1}{3}\,\partial_i(L_\rho^{-1}\,u_3)\right) - f_i\,, \quad \text{in } \Omega \times t > 0,\end{aligned} \tag{24}$$

$$f_i = \rho^{(0)}\,\frac{T^{(1)}}{T^{(0)}}\,\delta_{i3} - \rho^{(0)}\,\frac{2\,At\,c^{(1)}}{1 + At - 2\,At\,c^{(0)}}\,\delta_{i3}, \tag{25}$$

with the constraint

$$\partial_i u_i = -L_\rho^{-1} u_3 \quad \text{in}\,\overline{\Omega}, \tag{26}$$

with Dirichlet boundary conditions for the two velocity components on each subdomain. Here the change of variables (20) has not yet been performed. In these equations f_i is a known source term and $L_\rho^{-1} = {\rho^{(0)}}^{-1}\,d_z\rho^{(0)}$. There is no preferred direction in the (x, y)-horizontal plane, which allows us to reduce the Stokes problem to two dimensions, the second horizontal velocity component being solution of a Helmholtz problem. As a consequence, only one horizontal wave number is considered, i.e., $k = \sqrt{k_x^2 + k_y^2}$. We keep x as the resulting horizontal coordinate.

Inserting the decompositions (19) into (24) provides us with the Fourier version of the problem for each wave number k. Then the change of variables (20) is carried out. The resulting matrix system reads ($p^{(1)}$ is now written p)

$$\begin{aligned}\rho^{(0)}(z)\,\partial_t\begin{pmatrix}\widetilde{v}_k\\ \widetilde{w}_k\end{pmatrix} &= -\mathcal{G}_{A\,k}\,\widetilde{p}_k + \frac{1}{Re}\mathcal{L}_{A\,k}\begin{pmatrix}\widetilde{v}_k\\ \widetilde{w}_k\end{pmatrix} + \begin{pmatrix}\widetilde{s}_{v,k}\\ \widetilde{s}_{w,k}\end{pmatrix}, \\ \rho^{(0)}(z)\,\partial_t\widetilde{v}_k^{\perp} &= Re^{-1}\,(\partial_{zz}^2 - k^2)\widetilde{v}_k^{\perp} + \widetilde{s}_{v,k}^{\perp}.\end{aligned} \tag{27}$$

At this stage $\widetilde{v}_k$, $\widetilde{w}_k$, $\widetilde{v}_k^{\perp}$, $\widetilde{p}_k$, $\widetilde{s}_{v,k}$, $\widetilde{s}_{w,k}$ and $\widetilde{s}_{v,k}^{\perp}$ depend on (z, t). The operators $\mathcal{G}_{A\,k}$ and $\mathcal{L}_{A\,k}$ are defined as

$$\begin{aligned}\mathcal{G}_{A\,k} &= \begin{pmatrix} k\,Sr^{-1} \\ Sr^{-1}\,\partial_z + \rho^{(0)}/p^{(0)}\end{pmatrix}, \\ \mathcal{L}_{A\,k} &= \begin{pmatrix}\partial_{zz}^2 - k^2 & \frac{1}{3}\,k\,L_\rho^{-1} \\ 0 & \partial_{zz}^2 - k^2 - \frac{1}{3}\,d_z L_\rho^{-1} - \frac{1}{3}\,L_\rho^{-1}\,\partial_z\end{pmatrix},\end{aligned} \tag{28}$$

and

$$k\,\widetilde{v}_k + \left(\partial_z + L_\rho^{-1}\right)\widetilde{w}_k = 0, \tag{29}$$

where $\widetilde{s}_{v,k}$ and $\widetilde{s}_{v,k}^{\perp}$ are obtained using the change of variables (20) applying on the source term $s_i = f_i - \rho^{(0)}(z)\,u_j\,\partial_j u_i$, written in the Fourier space. As $w \equiv u_3$ we have $\widetilde{s}_{w,k} \equiv \widetilde{s}_{3,k}$. The inertia term is considered as a source since it is explicitly handled. Notice that equation (29) allows us to express $\widetilde{v}_k$ in terms of $\widetilde{w}_k$, when k is different from zero. The case $k = 0$ requires therefore a particular attention. This will be treated later and k is considered for the moment as being non-zero.

3.2. Time discretization

The system (27) is time discretized by applying the Runge–Kutta scheme. Three intermediate times t_q, $q = 1, 2, 3$, are introduced, such that $t_n < t_1 < t_2 < t_3 = t_{n+1} = t_n + \Delta t$. For each q a matrix system can be established

$$\begin{aligned}\left[\rho^{(0)}(z)\,\frac{\Gamma_q}{\Delta t}I_2 - \frac{1}{Re}\mathcal{L}_{A\,k}\right]\begin{pmatrix}\widetilde{v}_k^{(q+1)}\\ \widetilde{w}_k^{(q+1)}\end{pmatrix} + \mathcal{G}_{A\,k}\,\widetilde{p}_k^{(q+1)} &= \begin{pmatrix}\widetilde{s}_{u,k}^{(q)}\\ \widetilde{s}_{w,k}^{(q)}\end{pmatrix}, \\ \left[\rho^{(0)}(z)\frac{\Gamma_q}{\Delta t} - Re^{-1}(\partial_{zz}^2 - k^2)\right]\widetilde{v}_k^{\perp(q+1)} &= \widetilde{s}_{v,k}^{\perp(q)},\end{aligned} \tag{30}$$

where I_N is the $N \times N$ identity matrix. The Γ_q's are the three-step Runge–Kutta coefficients: $\Gamma_1 = 1/6$, $\Gamma_2 = 5/24$ and $\Gamma_3 = 1/8$. The superscript (q) stands for the number of the time subcycle. The updated source terms are written $\widetilde{\bullet}_{,k}^{(q)}$, with $\bullet = s_v, s_w, s_v^\perp$. At this stage $\widetilde{v}_k^{(q)}$, $\widetilde{w}_k^{(q)}$, $\widetilde{v}_k^{\perp(q)}$, $\widetilde{p}_k^{(q)}$, $\widetilde{s}_{v,k}^{(q)}$, $\widetilde{s}_{w,k}^{(q)}$ and $\widetilde{s}_{v,k}^{\perp(q)}$ only depend on z. Notice that the equation for $v^\perp$ is a Helmholtz equation, just like the concentration and temperature equations. The solution of these three equations is thus very similar. The pressure amplitudes, $\widetilde{p}_k^{(q+1)}$, are evaluated at each time subcycle in such a way that the following version of Eq. (29)

$$k\widetilde{v}_k^{(q+1)} + \left(d_z + L_\rho^{-1}\right)\widetilde{w}_k^{(q+1)} = 0, \qquad \forall z \in [z_a^{(m)}, z_b^{(m)}], m = 1, \ldots, M, \tag{31}$$

is satisfied at all the z-nodes.

3.2.1. Matching conditions and influence matrix method

Equations for v, w As we have already said, the matching of velocity, temperature, and concentration is performed with the influence matrix technique where the solution v, w, and p are sought under the form

$$\widetilde{\phi}_k^{(q+1)} = \widetilde{\phi}_k^{(q+1)(0)} + \sum_{s=1}^{4} \lambda_s^\phi \, \widetilde{\phi}_k^{(q+1)(s)}. \tag{32}$$

The first term $\widetilde{\phi}_k^{(q+1)(0)}$ is the solution to the problem with the source term and homogeneous boundary conditions. The $\widetilde{\phi}_k^{(q+1)(s)}$ $(s = 1, 2, 3, 4)$ are the solutions of the homogeneous problems and with non-zero Dirichlet boundary conditions. The matching conditions and the boundary conditions lead to an algebraic linear system for the λ_s^ϕ. The differential problem (30) for $\widetilde{v}_k$ and $\widetilde{w}_k$ is solved with or without the source term (i.e. $s = 0$ and $s \neq 0$ respectively), and with the following boundary conditions:

$$\begin{aligned} &\widetilde{v}_k^{(q+1)(s)}(z = z_a^{(m)}) = \delta_{1s}, \qquad \widetilde{v}_k^{(q+1)(s)}(z = z_b^{(m)}) = \delta_{2s}, \\ &\widetilde{w}_k^{(q+1)(s)}(z = z_a^{(m)}) = \delta_{3s}, \qquad \widetilde{w}_k^{(q+1)(s)}(z = z_b^{(m)}) = \delta_{4s}, \end{aligned} \tag{33}$$

where δ is the Kronecker symbol and for $m = 1, \ldots, M$.

Equations for $v^\perp$, c and T These three quantities are scalars and are solved in a similar way to the two velocity components (v, w), with only $s = 0, 1, 2$.

3.3. Space discretization

The set of equations (30)–(31) is now discretized along the z-direction using the Chebyshev collocation method [12,28,46]. Each of the unknown fields, $\widetilde{v}_k^{(q)}$, $\widetilde{w}_k^{(q)}$, $\widetilde{v}_k^{\perp(q)}$, $\widetilde{p}_k^{(q)}$, $\widetilde{T}_k^{(q)}$ and $\widetilde{c}_k^{(q)}$ is determined through a polynomial approximation which is denoted in the same way. A general distribution of collocation points is given by the set of M subdomains with $N_z + 1$ points, $[z_a^{(m)}, z_b^{(m)}]$, $m = 1, \ldots, M$. A coordinate transform is used in each subdomain $z^{(m)}(\xi) = f^{(m)}(\xi; a^{(m)})$, which depends on a unique real parameter denoted $a^{(m)}$. For this study, the following transform was found to yield satisfactory results

$$f^{(m)}(\xi; a^{(m)}) = (z_a^{(m)} + z_b^{(m)})/2 + a^{(m)}\,\xi\,(1 + {b^{(m)}}^2 - \xi^2)^{-1/2}, \; a^{(m)} \geq 0, \tag{34}$$

where $b^{(m)} = 2a^{(m)}/(z_b^{(m)} - z_a^{(m)})$. Let us list the parameters which define the grid. The location of the boundaries of the subdomains are defined by $M - 1$ real parameters and there are M real parameters associated with the coordinate transforms (34). As a result, the set of collocation points is defined by $2M - 1$ parameters. These parameters are dynamically adapted as detailed in Section 3.7. On the other hand, let D_{CGL} be the first-derivation Chebyshev Gauss–Lobatto matrix, of size $(N_z + 1)$, whose entries are given for example in [12]. The first-derivative physical space matrix is $D = {f'}^{-1} D_{CGL}$. The second-derivation matrix is D^2.

Let us introduce a set of column vectors, $\widetilde{V}_k^{(q)(s)}$, $\widetilde{W}_k^{(q)(s)}$, $\widetilde{V}_k^{\perp(q)(s)}$ and $\widetilde{P}_k^{(q)(s)}$, made of the $(N_z + 1)$ nodal values of $\widetilde{v}_k^{(q)(s)}(z)$, $\widetilde{w}_k^{(q)(s)}(z)$, $\widetilde{v}_k^{\perp(q)(s)}(z)$ and $\widetilde{p}_k^{(q)(s)}(z)$, respectively. They are defined, for example, by

$$\widetilde{P}_k^{(q)(s)} \equiv (\widetilde{p}_{k,0}^{(q)(s)} \; \ldots \; \widetilde{p}_{k,N_z}^{(q)(s)})^T \;\text{ with }\; \widetilde{p}_{k,n}^{(q)(s)} \equiv \widetilde{p}_k^{(q)(s)}(z_n),$$

where the superscript (m) has been omitted for the sake of clarity. Then the matrix D is such that, for example,

$$\widetilde{V'}_k^{(q)(s)} = D\,\widetilde{V}_k^{(q)(s)}. \tag{35}$$

This equation yields the first derivative of $\widetilde{v}_k^{(q)(s)}(z)$ evaluated at the $(N_z + 1)$ points, i.e., the $\frac{d}{dz}\widetilde{v}_k^{(q)(s)}\Big|_{z_p}$'s which constitute the column vector $\widetilde{V'}_k^{(q)(s)}$. Notice that all the eigenvalues of the matrix D are zero. This makes it impossible to invert, which is not surprising as it would mean that a differential problem could be solved without imposing boundary conditions.

According to the boundary conditions (33), the column vectors $\widetilde{V}_k^{(q)(s)}$, $\widetilde{W}_k^{(q)(s)}$ and $\widetilde{V}_k^{\perp(q)(s)}$ have only (N_z-1) unknown entries. This suggests that the internal nodal values of $\widetilde{v}_k^{(q)(s)}(z)$, $\widetilde{w}_k^{(q)(s)}(z)$ and $\widetilde{v}_k^{\perp(q)(s)}(z)$ are the true velocity unknowns of the problem. Let us thus express the entire discretized system in terms of these unknowns, following the approach described in [34]. Once the internal nodal values are determined, the boundary values are fixed using equations (33). We are thus led to introduce the 'internal' column vectors $\widetilde{V}_{k,I}^{(q)(s)}$, $\widetilde{W}_{k,I}^{(q)(s)}$ and $\widetilde{V}_{k,I}^{\perp(q)(s)}$ defined, for example, as

$$\widetilde{V}_{k,I}^{(q)(s)} \equiv (\widetilde{v}_{k,1}^{(q)(s)} \ \dots \ \widetilde{v}_{k,N_z-1}^{(q)(s)})^T.$$

3.3.1. Discretization of the momentum equation

Equations for v, w We are now ready to discretize the system (30), whose first equation leads to the following block-matrix system,

$$L_{Ak}\begin{pmatrix}\widetilde{V}_{k,I}^{(q+1)(s)}\\ \widetilde{W}_{k,I}^{(q+1)(s)}\end{pmatrix} + G_{Ak}\,\widetilde{P}_k^{(q+1)(s)} = \begin{pmatrix}\widetilde{S}_{v,k}^{(q)}\,\delta_{0s} + \widetilde{\Sigma}_{v,k}^{(q)(s)}\\ \widetilde{S}_{w,k}^{(q)}\,\delta_{0s} + \widetilde{\Sigma}_{w,k}^{(q)(s)}\end{pmatrix}, \tag{36}$$

where $s = 0, \dots, 4$. The operators G_{Ak} and L_{Ak} are given by

$$L_{Ak} = \begin{pmatrix} H_{Vk} & -\frac{k}{3}\frac{L_\rho^{-1}{}_I}{Re}\,I_{N_z-1}\\ 0 & H_{Wk}\end{pmatrix} \quad \text{and} \quad G_{Ak} = \begin{pmatrix}\frac{k}{Sr}\,\underline{I}\\ \frac{1}{Sr}\,\underline{D} + \frac{\rho^{(0)}}{p^{(0)}}\underline{I}\end{pmatrix}, \tag{37}$$

where H_{Vk} and H_{Wk} are square matrices of size (N_z-1). They are elliptic operators, therefore invertible and are expressed by the following relations

$$\begin{aligned} H_{Vk} &= \frac{\Gamma_q}{\Delta t}\rho_I - \frac{1}{Re}\left(-k^2\,I_{N_z-1} + D_I^2\right),\\ H_{Wk} &= \frac{\Gamma_q}{\Delta t}\rho_I - \frac{1}{Re}\left[-k^2\,I_{N_z-1} + D_I^2 - \frac{1}{3}(\,D_I L_\rho^{-1}{}_I + L_\rho^{-1}{}_I D_I)\right], \end{aligned} \tag{38}$$

where

1. the diagonal matrices ρ_I and $L_\rho^{-1}{}_I$ are of size (N_z-1); the ρ_I non-zero elements are $(\rho_I)_{jj} = \rho^{(0)}(z_j)$, $j = 1, \dots, N_z-1$,
2. $\underline{I}$ and $\underline{D}$ are rectangular matrices, of (N_z-1) rows and (N_z+1) columns, whose elements are defined by

$$\left.\begin{aligned}\underline{I}_{\nu n} &= \left(I_{N_z+1}\right)_{\nu n}\\ \underline{D}_{\nu n} &= D_{\nu n}\end{aligned}\right\}, \quad \text{for} \quad \begin{cases} n = 0, \dots, N_z\\ \nu = 1, \dots, N_z-1,\end{cases}$$

3. D_I is an $(N_z-1)\times(N_z-1)$ matrix and is the inner part of D

$$D_I(i,j) = D(i,j), \qquad 1 < i, j < N_z - 1.$$

4. $\widetilde{S}_{u,k}^{(q)}$ and $\widetilde{S}_{w,k}^{(q)}$ are column vectors of length (N_z-1) which are composed of the internal nodal values of the right-hand-side of the first equation of system (30).
5. $\widetilde{\Sigma}_{u,k}^{(q)(s)}$ and $\widetilde{\Sigma}_{w,k}^{(q)(s)}$ are source terms due to the boundary conditions (33). Their expression is given in Appendix A.

Equation for $v^\perp$ Similarly we get an equation for the internal nodal values of $\widetilde{V}_k^{\perp(q)(s)}$, which is a Helmholtz equation

$$\left[\rho_I\frac{\Gamma_q}{\Delta t} - Re^{-1}(D_I^2 - k^2 I_{N_z-1})\right]\widetilde{V}_{k,I}^{\perp(q+1)(s)} = \widetilde{S}_{v,k}^{\perp(q)}\delta_{0s} + \widetilde{\Sigma}_{v,k}^{\perp(q)(s)}, \tag{39}$$

where $s = 0, \dots, 2$. The source term $\widetilde{\Sigma}_{v,k}^{\perp(q)(s)}$ is related to the boundary conditions and its expression is given in Appendix A.

Let us now build the pressure operator.

3.3.2. Discretization of the constraint equation $\partial_i\left(\rho^{(0)}(z)\,u_i\right) = 0$

The discrete version of (31) directly reads

$$k\,\widetilde{V}_k^{(q+1)(s)} + \left(D + L_\rho^{-1}\,I_{N_z+1}\right)\widetilde{W}_k^{(q+1)(s)} = 0. \tag{40}$$

This relation is now modified to be expressed in terms of the internal column vectors $\widetilde{V}_{k,I}^{(q+1)(s)}$ and $\widetilde{W}_{k,I}^{(q+1)(s)}$. To this end we need to introduce two rectangular matrices, with (N_z+1) rows and (N_z-1) columns. They are $\bar{I}$ and $\overline{D}$, defined by

$$\left.\begin{aligned}\bar{I}_{n\nu} &= \left(I_{N_z+1}\right)_{n\nu}\\ \overline{D}_{n\nu} &= D_{n\nu}\end{aligned}\right\}, \quad \text{for} \quad \begin{cases} n = 0, \dots, N_z\\ \nu = 1, \dots, N_z-1.\end{cases}$$

These matrices allow us to write down the matrix form of the discrete version of $\partial_i\left(\rho^{(0)}(z)\,u_i\right)=0$ (see equation (40)), which involves only the internal nodal values of the velocity. The boundary terms of the velocity are determined by the boundary conditions (33). Finally the constraint equation writes

$$k\,\bar{I}\,\widetilde{V}_{k,I}^{(q+1)(s)}+\left(\overline{D}+L_\rho^{-1}\,\bar{I}\right)\widetilde{W}_{k,I}^{(q+1)(s)}=-\Sigma_{Dw}^{(q)(s)}-\Sigma_{vw}^{(q)(s)}, \tag{41}$$

where the source terms, $\Sigma_{Dw}^{(q)(s)}$ and $\Sigma_{vw}^{(q)(s)}$, are given in Appendix A.

3.3.3. Uzawa equation on the pressure

We are now able to construct the Uzawa operator $A_{P\,k}$ acting on the pressure, which allows equation (41) to be satisfied at the z-nodes. It writes

$$A_{P\,k}\,\widetilde{P}_k^{(q+1)(s)}=F_{P\,k}^{(q)(s)}. \tag{42}$$

To this end we proceed in three steps, *i*) expressing from (36) the column vectors $\widetilde{V}_{k,I}^{(q+1)(s)}$ and $\widetilde{W}_{k,I}^{(q+1)(s)}$ in terms of $\widetilde{P}_k^{(q+1)(s)}$, *ii*) injecting these terms in equation (41) and finally *iii*) identifying the operator $A_{P\,k}$ and the r.h.s. $F_{P\,k}^{(q)(s)}$. The first step leads to the following matrix expressions,

$$H_{V\,k}\,\widetilde{V}_{k,I}^{(q+1)(s)}=F_{V\,k}^{(q)(s)},$$

with

$$\begin{aligned}F_{V\,k}^{(q)(s)}=&-k\left[\frac{L_\rho^{-1}{}_I}{3\,Re}\,H_{W\,k}^{-1}\left(\frac{1}{Sr}\,\underline{D}+\frac{\rho^{(0)}}{p^{(0)}}\underline{I}\right)+\frac{1}{Sr}\,\underline{I}\right]\widetilde{P}_k^{(q+1)(s)}\\&+\widetilde{S}_{v,k}^{(q)}\,\delta_{0s}+\widetilde{\Sigma}_{v,k}^{(q)(s)}+\frac{k}{3}\,\frac{L_\rho^{-1}{}_I}{Re}\,H_{W\,k}^{-1}\left(\widetilde{S}_{w,k}^{(q)}\,\delta_{0s}+\widetilde{\Sigma}_{w,k}^{(q)(s)}\right),\end{aligned} \tag{43}$$

and

$$H_{W\,k}\,\widetilde{W}_{k,I}^{(q+1)(s)}=-\left(\frac{1}{Sr}\,\underline{D}+\frac{\rho^{(0)}}{p^{(0)}}\underline{I}\right)\widetilde{P}_k^{(q+1)(s)}+\widetilde{S}_{w,k}^{(q)}\,\delta_{0s}+\widetilde{\Sigma}_{w,k}^{(q)(s)}. \tag{44}$$

The resulting $A_{P\,k}$ matrix reads

$$\begin{aligned}A_{P\,k}=&-k^2\,\bar{I}\,H_{V\,k}^{-1}\left[\frac{L_\rho^{-1}{}_I}{3\,Re}H_{W\,k}^{-1}\left(\frac{1}{Sr}\,\underline{D}+\frac{\rho^{(0)}}{p^{(0)}}\underline{I}\right)+\frac{1}{Sr}\,\underline{I}\right]\\&-\left(\overline{D}+L_\rho^{-1}\,\bar{I}\right)H_{W\,k}^{-1}\left(\frac{1}{Sr}\,\underline{D}+\frac{\rho^{(0)}}{p^{(0)}}\underline{I}\right),\end{aligned} \tag{45}$$

together with the right-hand side $F_{P\,k}^{(q)(s)}$

$$\begin{aligned}F_{P\,k}^{(q)(s)}=&-k\,\bar{I}\,H_{V\,k}^{-1}\left[\frac{k}{3}\,\frac{L_\rho^{-1}{}_I}{Re}\,H_{W\,k}^{-1}\left(\widetilde{S}_{w,k}^{(q)}\,\delta_{0s}+\widetilde{\Sigma}_{w,k}^{(q)(s)}\right)+\widetilde{S}_{v,k}^{(q)}\,\delta_{0s}+\widetilde{\Sigma}_{v,k}^{(q)(s)}\right]\\&-\left(\overline{D}+L_\rho^{-1}\,\bar{I}\right)H_{W\,k}^{-1}\left(\widetilde{S}_{w,k}^{(q)}\,\delta_{0s}+\widetilde{\Sigma}_{w,k}^{(q)(s)}\right)-\Sigma_{Dw}^{(q)(s)}-\Sigma_{vw}^{(q)(s)}.\end{aligned} \tag{46}$$

3.3.4. The $k\neq 0$ anelastic-Uzawa pressure operator properties

There is no spurious pressure modes in the $k\neq 0$ anelastic configuration (cf. [34]). This implies the ellipticity of $A_{P\,k\neq 0}$. Actually its eigenvalues λ_n, for $n=1,\ldots,N_z+1$, are all positive. Fig. 3 (left) shows a plot of the $\log_{10}(\lambda_n)$'s obtained with $N_z=50$, for $Re=10^4$, $k=2\pi$ and $Sr=1$. A typical arbitrary value $\Gamma_q/\Delta t=10^3$ has been chosen for the computation of the eigenvalues. Defining the condition number of $A_{P\,k\neq 0}$ by $\kappa=\frac{\max_n\lambda_n}{\min_n\lambda_n}$, one gets its numerical estimate as a function of N_z from the plot shown in Fig. 3 (right). The measured slope is 3.95, which suggests the asymptotic law $\kappa\propto N_z^4$.

3.3.5. The $k=0$ case

Fixing k to zero amounts to suppressing any x-dependence from the problem. In that case the constraint equation (5) tells us that $\partial_z(\rho^{(0)}(z)\,\widetilde{w}_0)=0$. This along with the w-boundary condition given in (11) implies that

$$\widetilde{w}_0(z,t)=0.$$

Taking this into account and putting $k=0$ in equations (30) provides us with a new system which reads

$$\left[\rho^{(0)}(z)\,\partial_t-Re^{-1}\partial_{zz}^2\right]\widetilde{v}_0=\widetilde{s}_{v,0}, \tag{47}$$

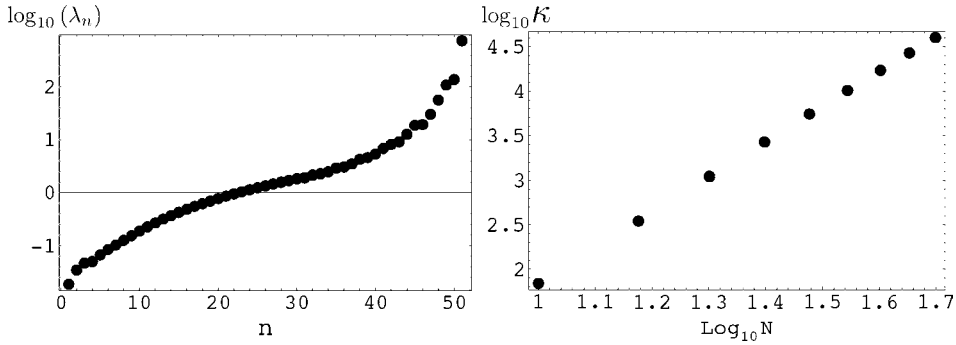

Fig. 3. Left: Eigenvalues of the Uzawa operator $A_{P\,k\neq 0}$, via the $\log_{10}(\lambda_n)$'s, obtained $N_z = 50$, for $Re = 10^4$, $\Gamma_q/\Delta t = 10^3$, $k = 2\pi$ and $Sr = 1$. Right: Condition number κ, via $\log_{10}(\kappa)$, of the Uzawa operator $A_{P\,k\neq 0}$ obtained as a function of N_z (same parameter values).

and

$$\left(\frac{1}{Sr}\,\partial_z + \frac{\rho^{(0)}}{p^{(0)}}\right)\widetilde{p}_0 = \widetilde{s}_{w,0}. \tag{48}$$

Equation (47) is closed by the following boundary conditions:

$$\partial_z \widetilde{v}_0|_{z=z_b,z_t} = 0. \tag{49}$$

The unknown fields $\widetilde{v}_0(z,t)$ and $\widetilde{p}_0(z,t)$ are now decoupled. The velocity $\widetilde{v}_0$ is governed by a linear unsteady heat equation with no-flux (no-stress) conditions. The pressure $\widetilde{p}_0$ is governed by an inhomogeneous hydrostatic equation posed on the entire domain (boundaries included), since the pressure is defined everywhere. The discretization of the pressure step deserves some comments since equation (48) can be solved in different ways.

1. It might be tempting to discretize this equation and invert the resulting matrix. This is probably not a good option. Inverting matrices made of the first-derivation matrix D often leads to difficulties, such as departure from the exponential convergence that one expects in the results, [28];
2. it should be noticed that equation (48) possesses an analytical solution

$$\widetilde{p}_0(z,t) = \left(\widetilde{P}_0(t) + Sr\int_{z_b}^{z} \widetilde{s}_{w,0}(\eta,t)\,\mathrm{e}^{g(\eta)}d\eta\right)\mathrm{e}^{-g(z)}, \tag{50}$$

   where

$$g(z) = Sr\int_{z_b}^{z} \frac{\rho^{(0)}(\lambda)}{p^{(0)}(\lambda)}d\lambda, \tag{51}$$

   and $\widetilde{P}_0(t)$ is a constant of integration. Its determination is obtained by imposing the total mass conservation;
3. finally, as proposed in [46], one may invert the Uzawa operator $A_{P\,k=0}$ that one obtains by setting k to zero in the operator given in (45).

The solution methods 2 and 3 have been tested on several 2D simulations with several spatial resolutions and various values of the stiffness parameter δ (equation (13)). It was found that the inversion of the Uzawa operator gives slightly better results for smooth density gradients (large values of δ) and much better results for stiff density gradients (small values of δ). Since RT-configurations are typically stiff, we have preferred solution 3, the inversion of the Uzawa operator. The pressure $\widetilde{p}_0$ is then matched in the following way. As mentioned in Section 2.1, the solution $\widetilde{p}_0$ of equation (48) is determined up to an additive function, which is proportional to the mean pressure $p^{(0)}$. By using this invariance of the dynamic pressure, the matching condition of the pressure between two subdomains is

$$\widetilde{p}_0^{(m)} + \alpha_p^{(m)}\,p^{(0)} = \widetilde{p}_0^{(m+1)} + \alpha_p^{(m+1)}\,p^{(0)} \qquad m = 1,\ldots,M-1. \tag{52}$$

The Mth equation is provided by the conservation of mass $\int \rho\,dV = const$. Since Fourier basis functions are used in the horizontal direction, this constraint simply writes

$$\sum_{m=1}^{M}\int_{z_a^{(m)}}^{z_b^{(m)}} \rho_0^{(m)}(z)\,dz = 0, \tag{53}$$

where the density fluctuation is written is terms of the pressure fluctuation.

3.4. Consistency

As indicated in Table 1, the Uzawa uncoupling method, designed for the Boussinesq–Stokes approximation, is consistent with the continuous decoupled version of the system. This well-known property comes from the fact that the Uzawa uncoupling is a direct numerical translation of the problem, i.e., of its differential part and of its boundary conditions. This conclusion also holds for the anelastic approximation.

More precisely for the Boussinesq case, the continuous velocity–pressure uncoupling leads to Poisson and heat equations acting on the pressure and on $\partial^2_{jj} u_i$, respectively. It was found by Karniadakis et al. [32] that the uncoupling achieved through the time-splitting schemes amounts to introducing an additional multiplicative space-time operator to these two equations. This was further analyzed by Leriche and Labrosse [36]. These schemes are therefore not consistent with the continuous uncoupled formulation of the initial problem. In particular, the pressure is governed by an operator involving time, which contradicts the incompressibility hypothesis. A simple example of inconsistent algorithm is also provided by the Du Fort and Frankel scheme applied to the heat equation. Indeed it has been shown that this scheme is consistent with a hyperbolic equation ([48], Section 7.5).

3.5. Iterative procedures

The linear systems for the pressure (42) and the two velocity components (43)–(44) as well as the Helmholtz problems arising from the solution of the equation for the second horizontal velocity (39), the internal energy (8) and the concentration (9) may be solved by direct inversion. They also may be solved with iterative procedures. Both methods have been tested. As expected, iterative methods are more accurate and more robust than direct methods. They are also much less memory-consuming, which is a great advantage on most recent supercomputers. The pressure $\widetilde{P}_k^{(q+1)}$ is first calculated. The velocities $\widetilde{V}_{k,I}^{(q+1)(s)}$ and $\widetilde{W}_{k,I}^{(q+1)(s)}$, whose calculation needs $\widetilde{P}_k^{(q+1)}$, follow. The velocity $\widetilde{V}_{k,I}^{\perp(q+1)(s)}$, concentration and temperature Helmholtz equations can be solved independently.

3.5.1. Pressure

There is no obvious preconditioner to the Uzawa operator, therefore the pressure is solved in two steps: first the inverse operator $A_{P\,k}^{-1}$ is directly computed. In a second step, this inverse is used as a preconditioning for the Richardson iterations over ℓ

$$\widetilde{P}_{k\,(\ell+1)} = \widetilde{P}_{k\,(\ell)} + \alpha_R\, A_{P\,k}^{-1} (A_{P\,k} \widetilde{P}_{k\,(\ell)} - \widetilde{f}_k), \tag{54}$$

where the time cycle superscript (q) has been omitted. As the pressure operator is ill-conditioned, the direct inversion generates numerical errors. The idea of the Richardson iterations is to refine the solution and reduce these errors. The spectra of the operator $A_{P\,k}^{-1} A_{P\,k}$ is very closed to 1, indeed departures are only due to numerical errors, and the relaxation parameter is fixed to a large value, $\alpha_R = 0.95$. The convergence is achieved very quickly and only 3 to 6 iterations are performed. The residual of a small minority of modes does not reach 10^{-12} after the direct inversion. These residuals are decreased by 2 to 4 orders of magnitude during the Richardson iterative stage. In the end, nearly all modes reach a residual of 10^{-12}.

3.5.2. Coupled velocities

Since Chebyshev collocation methods result in non-symmetric operators, we chose the so-called 'Chebyshev acceleration method' [45] even if methods designed for symmetric problems work well in the non-symmetric cases [20]. This scheme writes

$$\varphi_{(\ell+1)} = \omega_\ell\, \varphi_{(\ell)} + (1-\omega_\ell)\, \varphi_{(\ell-1)} + \alpha_{Ch}\, \omega_\ell\, L_{A\,prec}^{-1} (L_A \varphi_{(\ell)} - f). \tag{55}$$

The variable φ stands for the column vector $(\widetilde{V}_{k,I}^{(q)}\ \widetilde{W}_{k,I}^{(q)})^T$. Indeed the two velocities $\widetilde{V}_{k,I}^{(q)}$ and $\widetilde{W}_{k,I}^{(q)}$ are coupled and solved simultaneously (equation (36)). In this case, the operator L_A is a 2×2 block-operator whose diagonal elements are the $H_{V\,k}$ and $H_{W\,k}$ operators (see equation (38)) and the sole non-zero off-diagonal element is $L_{A\,12} = -k\, L_\rho^{-1}{}_I\, I_{N_z-1}/3\,Re$, due to the non-zero velocity divergence. This operator is preconditioned by a block diagonal operator $L_{A\,prec}$ [21], whose diagonal blocks are the tridiagonal finite-volume approximation [35] of the operators $H_{V\,k}$ and $H_{W\,k}$. The relaxation parameter α_{Ch} has been calibrated to $\alpha_{Ch} = 0.98$. Convergence is considered to be achieved when the residual reaches 10^{-12}. At the beginning of a simulation, the number of iterations needed to reach convergence is about 30 for $(\widetilde{V}_{k,I}^{(q)}\ \widetilde{W}_{k,I}^{(q)})^T$. As the calculation progresses, the number of iterations needed for convergence drops since the time step and the stiffness of the initial density gradient decrease. For example, after 6,500 time cycles ($t = 8.47$), 14 iterations are performed for the coupled velocities.

3.5.3. Horizontal velocity, concentration and temperature

All three horizontal velocity, concentration and temperature equations are Helmholtz equations. The calculation is carried out using the iterative method (equation (55)) with the same relaxation parameter value used in the coupled-velocity case. The number of iterations needed for convergence is around 20 at the beginning of a simulation and constantly drops when simulation time goes on: 11 iterations after 6500 time cycles in the same example as above.

3.6. Solution method for the Boussinesq model

From a mathematical point of view, the Boussinesq system is close to the set of equations (7)–(10). The velocity and the pressure are the solution of a Stokes problem, the concentration equation is identical to equation (9), and the temperature equation is removed. Note that the pressure p involved here is a pure Lagrangian multiplier, which ensures that the constraint $\partial_i u_i = 0$ is satisfied. The various operators involved in the numerical algorithm simplify themselves since $L_\rho^{-1} = 0$.

3.6.1. Uzawa equations for velocity and pressure

The operators $H_{V\,k}$ and $H_{W\,k}$ are identical $H_{V\,k} = H_{W\,k} \equiv H_k$. The equations on $\widetilde{V}_{k,I}^{(q+1)(s)}$ and $\widetilde{W}_{k,I}^{(q+1)(s)}$ are no longer coupled. Within the Boussinesq approximation, system (36) and equation (39) write

$$\begin{aligned}
&H_k\,\widetilde{V}_{k,I}^{(q+1)(s)} + k\,\underline{I}\,\widetilde{P}_k^{(q+1)(s)} = \widetilde{S}_{v,k}^{(q)}\,\delta_{0s} + \widetilde{\Sigma}_{v,k}^{(q)(s)},\\
&H_k\,\widetilde{W}_{k,I}^{(q+1)(s)} + \underline{D}\,\widetilde{P}_k^{(q+1)(s)} = \widetilde{S}_{w,k}^{(q)}\,\delta_{0s} + \widetilde{\Sigma}_{w,k}^{(q)(s)},\\
&H_k\,\widetilde{V}_{k,I}^{\perp(q+1)(s)} = \widetilde{S}_{v,k}^{\perp(q)}\,\delta_{0s} + \widetilde{\Sigma}_{v,k}^{\perp(q)(s)},
\end{aligned} \tag{56}$$

where the source terms have been updated, and:

$$H_k = \frac{\Gamma_q}{\Delta t} - \frac{1}{Re}\left(-k^2\,I_{N-1} + D_I^2\right). \tag{57}$$

Since the continuity equation is now only $\partial_i u_i = 0$, equation (41) becomes

$$k\,\bar{I}\,\widetilde{V}_{k,I}^{(q+1)(s)} + \overline{D}\,\widetilde{W}_{k,I}^{(q+1)(s)} = -\Sigma_{Dw}^{(q)(s)} - \Sigma_{vw}^{(q)(s)}. \tag{58}$$

The equation on pressure is then much simpler and equations (42) and (45) become

$$\begin{aligned}
\left(k^2\,\bar{I}H_k^{-1}\underline{I} - \overline{D}H_k^{-1}\underline{D}\right)\widetilde{P}_k^{(q+1)(s)} = &-k\bar{I}H_k^{-1}\left(\widetilde{S}_{v,k}^{(q)}\,\delta_{0s} + \widetilde{\Sigma}_{v,k}^{(q)(s)}\right)\\
&- \overline{D}H_k^{-1}\left(\widetilde{S}_{w,k}^{(q)}\,\delta_{0s} + \widetilde{\Sigma}_{w,k}^{(q)(s)}\right) - \Sigma_{Dw}^{(q)(s)} - \Sigma_{vw}^{(q)(s)}.
\end{aligned} \tag{59}$$

3.6.2. The $k = 0$ case

The $k = 0$ pressure equation is $\partial_z \widetilde{p}_0 = \widetilde{s}_{w,0}$. The solution is determined up to an additive constant. The matching condition of the pressure between two subdomains writes

$$\widetilde{p}_0^{(m)} + \alpha_p^{(m)} = \widetilde{p}_0^{(m+1)} + \alpha_p^{(m+1)}, \qquad m = 1, \ldots, M-1, \tag{60}$$

which provide $M-1$ equations for M unknowns. Unlike the anelastic case, the conservation of mass does not provide any extra equation. Therefore the pressure is arbitrarily set to 1 at the lower boundary of the simulation box. Then there are enough equations to determine the pressure value in every collocation point.

Pressure filtering For $k = 0$, it is noticeable that the pressure $\widetilde{p}_0^{(m+1)}$ only appears through its z-derivative $\underline{D}\,\widetilde{P}_0^{(q+1)(s)}$. The last Chebyshev mode of the Boussinesq pressure is thus a spurious mode ([46], Section 7.3) and is consequently reset to zero at each time cycle.

3.7. Auto-adaptive multidomain method

The Uzawa algorithm is embedded in an auto-adaptive multidomain approach in order to follow the flow gradients as time evolves. Both the numerical interface locations and the mapping parameters (equation (34)) are dynamically adapted. This method is based on a classical theorem of convergence [12, Section 9.5], [46, Section 3.6]

$$||u - P_N u||_{H_\omega^p(-1,1)} \leq C N^{2p-\ell-\frac{1}{2}}\,||u||_{H_\omega^\ell(-1,1)}, \quad \text{for} \quad 1 \leq p \leq \ell, \tag{61}$$

where $P_N u$ is the N-order Chebyshev approximation of the function u in $H_\omega^\ell(-1,1)$, for some $\ell \geq 1$. The norm of the weighted Sobolev space of order p is defined by

$$||u||^2_{H_\omega^p(-1,1)} = \sum_{k=0}^{p} \int_{-1}^{+1} \left|u^{(k)}(\zeta)\right|^2 \omega(\zeta)\mathrm{d}\zeta. \tag{62}$$

The convergence result (61) means that the projection error in the H_ω^p-space is bounded by the H_ω^ℓ-norm of the function [6, 23,27]. Therefore the optimization consists in minimizing a functional defined as the H_ω^ℓ-norm of a chosen test function u. In practice [27], the value $\ell = 2$ has been shown to give good results, and one considers rather the functional based on the first derivative of the test function $\left|\left|u^{(1)}\right|\right|_{H_\omega^1(-1,1)}$. The dependence of this norm on the interface locations and the

mapping parameters is the key point. For multivariable problems, the test function Φ is built from the physical variables $\rho, u_i, \ldots$. Numerical experiments suggest that using the normalized sum of the variables usually gives good results. The total functional J_2 is therefore defined as

$$J_2[\Phi] = \sum_{m=1}^{M} J_{2,\omega}\left[\Phi^{(m)}\right], \tag{63}$$

where $\Phi^{(m)}$ is the restriction of the test function Φ on the mth subdomain. The functional over one subdomain is defined as

$$J_{2,\omega}[\Phi] = \left\| \frac{d\Phi}{d\xi} \right\|_{1,\omega}^2 = \sum_{i=1}^{2} \int_{-1}^{+1} \left| \frac{d^i \Phi}{d\xi^i} \right|^2 \omega(\xi)\, d\xi, \tag{64}$$

with $\omega(\xi) = \left(1-\xi^2\right)^{-1/2}$ and where mappings have been used so that the integral is computed on the Gauss–Lobatto collocation points. A simple and robust iterative procedure has been devised for determining the best interface locations and the best values of the mapping parameters ([47], [46], Section 8.3.4). This algorithm consists in calculating the functional (63) at some selected values around a subdomain interface. The best location for this interface is given by the minimum of the norm of the functional. Such a computation is performed for every interface and iterated until convergence. This operation is called a collocation point distribution adaptation and is performed each time the following criterion is fulfilled

$$\max_{m=1,\ldots,M} \left| \frac{J_2\left[\Phi^{(m)}\right]}{J_2^{ref}\left[\Phi^{(m)}\right]} - 1 \right| \geq \varepsilon, \tag{65}$$

where the reference value $J_2^{ref}\left[\Phi^{(m)}\right]$ is the value of the functional at the previous adaptation and ε is a given tolerance level. Inequality (65) means that as soon as the variation of the projection error is larger than the tolerance level, a redistribution of interface locations and collocation points is automatically triggered. In this way, adaptations are performed only when it is necessary, i.e., according to the criterion (65) since the interpolation introduces numerical errors (see for example, [23], figure 3). We observe that the frequency of this redistribution is typically 1 every 100–200 time cycles.

In this procedure the Chebyshev and Fourier cut-offs stayed constant. This will no longer be the case for the manual grid refinement procedure detailed in Section 3.8.

3.8. Grid modifications

For large-scale numerical simulations, it may be convenient to vary the spatial resolution during the calculation. For example, RT-flows need more and more collocation points as turbulence develops. A tool has therefore been designed for this purpose. It allows us to modify the cut-offs in Chebyshev or Fourier directions, to increase the number of subdomains as well as vary the number of MPI processes (see Section 4.5).

To increase the cut-offs in Chebyshev or Fourier directions, the spectrum in the Chebyshev or Fourier space is supplemented with zeros, up to the new cut-off. The physical variables are then rebuilt in the new physical space. To add a subdomain, one splits a subdomain into two with the same cut-off N_z and with a Gauss–Lobatto distribution of collocation points. The Chebyshev spectrum (for each Fourier mode) is used to built the Lagrange interpolation polynomial. This polynomial is used to interpolate the variable on the $(N_z+1)+(N_z+1)-1 = 2N_z+1$ collocation points. Since a simulation is usually made of several runs, a re-start file is built at the end of each run. These resolution changes are carried out on this file and are decided by first calculating the one-dimensional spectrum

$$\begin{aligned} &\Phi_{1D}^{(m)}(K) = \max_{K=k_x+k_y+n} \left| \widetilde{\Phi}^{(m)}(k_x, k_y, n) \right| \quad \text{for} \quad m = 1, \ldots, M \\ &\text{and} \quad -N_{x,y}/2 \leq k_{x,y} \leq N_{x,y}/2 - 1, \quad 0 \leq n \leq N_z, \end{aligned} \tag{66}$$

where $\widetilde{\Phi}^{(m)}$ is the Fourier-transform of the test function $\Phi^{(m)}$. If for some specific wavenumber $K_\star$, one gets

$$\Phi_{1D}(K_\star) \geq \varepsilon_{1D}, \tag{67}$$

where ε_{1D} is a given tolerance, a manual grid refinement is performed either in the Fourier or Chebyshev directions or by splitting a specific subdomain. These resolution changes are at most carried out 5 or 6 times during a simulation. Fig. 4 illustrates how the grid modifications (interface locations and grid refinement) affect the simulation's accuracy. Grey arrows show triggering(s) of the auto-adaptive algorithm. Interfaces between subdomains automatically move according to criterion (65). This causes a slight decrease of $\overline{|\partial_i(\rho^{(0)}u_i)|}^{xyz}$, i.e., an accuracy improvement. Several hundreds of auto-adaptations may occur during a simulation. As the linear growth of RTI does not require a large number of collocation points, the grid is set to be small at the beginning of a simulation. This allows to compute the linear stage at a low computational cost. When bubbles, spikes—and later a mixing layer—develop, more collocation points are needed. Those are added manually.

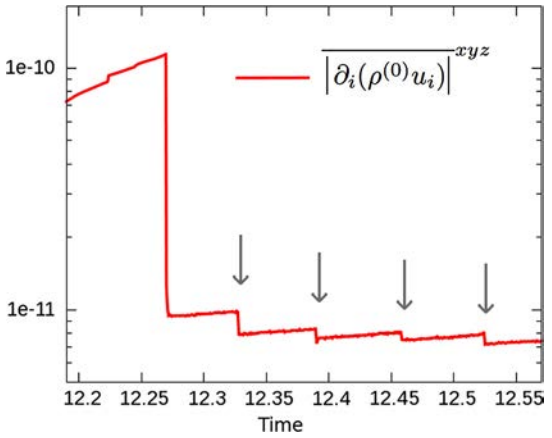

Fig. 4. Spatial average of the absolute value of the momentum divergence, $\overline{|\partial_i(\rho^{(0)}u_i)|}^{xyz}$, versus time for the 3D-anelastic simulation AM2 (Table 3). Grey arrows show times when grid adaptations were automatically performed by the algorithm. The drop of $\overline{|\partial_i(\rho^{(0)}u_i)|}^{xyz}$ at $t = 12.27$ is related to a manual grid refinement: before time $t = 12.27$ the grid is $[N_x, N_y, N_d \times (N_z + 1)] = [600, 600, (16 \times 48)]$ and after the resolution is $[816, 816, (20 \times 48)]$.

In the example in Fig. 4, at time $t = 12.27$, according to criterion (67) the grid is refined by adding around 35% Fourier modes in each horizontal direction and 25% Chebyshev modes. The quantity $\overline{|\partial_i(\rho^{(0)}u_i)|}^{xyz}$, which was increasing before the refinement, immediately drops by a factor 10 and stabilizes around 10^{-11} (see Fig. 4).

Finally the possible variation of the number of MPI processes is obtained by re-ordering the restart-file.

3.8.1. Time step control

Given a uniform grid defined by $(\Delta x, \Delta y, \Delta z)$, the stability CFL criteria for the Navier–Stokes equations classically writes

$$\Delta t \leq C \min_{i,j,k} \left[\frac{|u_{ijk}|}{\Delta x} + \frac{|v_{ijk}|}{\Delta y} + \frac{|w_{ijk}|}{\Delta z} \right]^{-1}. \tag{68}$$

Indeed when the diffusive part is treated implicitly, it does not lead to any constraint. Within the framework of spectral methods, it is convenient to express this criteria in terms of the cut-off wave numbers in the Fourier $(N_x,\ N_y)$ and the Chebyshev $(N_z + 1)$ directions

$$\Delta t \leq C \min_{m=1,M} \min_{i,j,k} \left[\frac{N_x}{2} \frac{\left|u_{ijk}^{(m)}\right|}{K_{Adv}^{Fou}} + \frac{N_y}{2} \frac{\left|v_{ijk}^{(m)}\right|}{K_{Adv}^{Fou}} + \frac{(N_z+1)^2}{\left|f^{(m)\prime}(\xi_k)\right|} \frac{\left|w_{ijk}^{(m)}\right|}{K_{Adv/Dir}^{Che}} \right]^{-1}, \tag{69}$$

where the factor $\left|f^{(m)\prime}(\xi_k)\right|$ comes from the coordinate transform in the Chebyshev direction. The coefficients $K_{Adv/Dir}^{Che}$ and K_{Adv}^{Fou} are determined through a stability analysis carried out on elementary equations. The coefficient $K_{Adv/Dir}^{Che}$'s value was fixed to 7.398 as determined by [9] in their full stability study on the Euler system. The coefficient K_{Adv}^{Fou} may be determined by considering a linear advection equation of the form $\partial_t u + U\,\partial_x u = 0$, where U is a constant and uniform velocity. The von Neumann condition for stability writes for a three-step Runge–Kutta scheme

$$\left| 1 - \mathrm{i}\,k\,U\,\Delta t - \frac{1}{2}(k\,U\,\Delta t)^2 + \frac{1}{6}\,\mathrm{i}\,(k\,U\,\Delta t)^3 \right|^2 \leq 1, \tag{70}$$

which leads to the constraint

$$\Delta t \leq \frac{\sqrt{3}}{k_{max}\,U} = K_{Adv}^{Fou}\,\frac{1}{U}\,\frac{L}{N_x/2} \quad \text{with} \quad K_{Adv}^{Fou} = \frac{\sqrt{3}}{2\pi} \approx 0.2757. \tag{71}$$

The global CFL coefficient C is taken equal to 0.9.

4. Numerical and computational features

This section is first devoted to the numerical features of the method, i.e., the spatial and temporal convergence and the optimal multidomain grid study. Computational features, such as parallelization efficiency and calculation times, are discussed. To seed an RT flow, a small velocity perturbation is added, such that $\partial_i(\rho^{(0)}u_i) = 0$ for the anelastic simulations and $\partial_i u_i = 0$ for the Boussinesq one. There are two main categories of velocity perturbations, which are characterized by their Fourier spectrum: single-mode (a single Fourier mode) or multi-mode. The latter is build with a set of Fourier

Table 3
List of the numerical simulations carried out for the validation and for the comparisons between the anelastic (AN) and the Boussinesq (BO) models. When manual grid refinement has been used, only the largest grid is given. For anelastic simulations, the adiabatic indexes are $\gamma_H = \gamma_L = 5/3$ and the Prandtl number is $Pr = 0.7$.

Case	Purpose	Model	Grid $M \times (N_z + 1) \times N_x \times N_y$	Interfaces	Parallelization $N_{cores} = M \times N_{MPI/d} \times N_{OMP/MPI}$	At	Sr	Re	Sc
GC	Grid convergence	AN	$(1 \times 32 \rightarrow 512) \times 1024$	fixed	$1 \times (16 \rightarrow 128) \times 1$	0.2	1	10^5	0.7
SD1	Optimal multidomain grid	"	$(1 \times 512) \times 1024$	"	$128 = 1 \times 128 \times 1$	0.1	1	"	"
SD2	"	"	$(2 \times 256) \times 1024$	"	$128 = 2 \times 64 \times 1$	0.1	1	"	"
SD3	"	"	$(4 \times 128) \times 1024$	"	$128 = 4 \times 32 \times 1$	0.1	1	"	"
SD4	"	"	$(4 \times 128) \times 1024$	"	$128 = 4 \times 32 \times 1$	0.1	1	"	"
SD5	"	"	$(4 \times 128) \times 1024$	mobile	$128 = 4 \times 32 \times 1$	0.1	1	"	"
SD6	"	"	$(8 \times 64) \times 1024$	"	$128 = 8 \times 16 \times 1$	0.1	1	"	"
AM1	Illustration CPU performance	"	$(12 \times 48) \times 600^2$	"	$576 = 12 \times 48 \times 1$	0.25	2	10^4	0.7
AM2	Grid refinement, spectra, model comparison	"	$(30 \times 48) \times 816^2$	"	$2880 = 30 \times 48 \times 2$	0.1	0.4	3×10^4	0.7
AS	Illustration	"	$(10 \times 64) \times 384^2$	"	$320 = 10 \times 32 \times 1$	0.2	0.2	5×10^3	0.7
AL	Linear growth rate temporal convergence	"	$(8 \times 48) \times 1536$	"	$128 = 8 \times 16 \times 1$	0.1	1	10^6	10^3
AT	Temporal convergence	"	$(6 \times 48) \times 128$	"	$48 = 6 \times 8 \times 1$	0.1	1	10^3	0.7
BW	Waddell et al. [55] exp.	BO	$(16 \times 64) \times 1536$	"	$128 = 16 \times 8 \times 1$	0.155	0	4970	6797
BM	Non-linear growth rate, model comparison	"	$(24 \times 40) \times 940^2$	"	$1920 = 24 \times 40 \times 2$	0.1	0	3×10^4	0.7

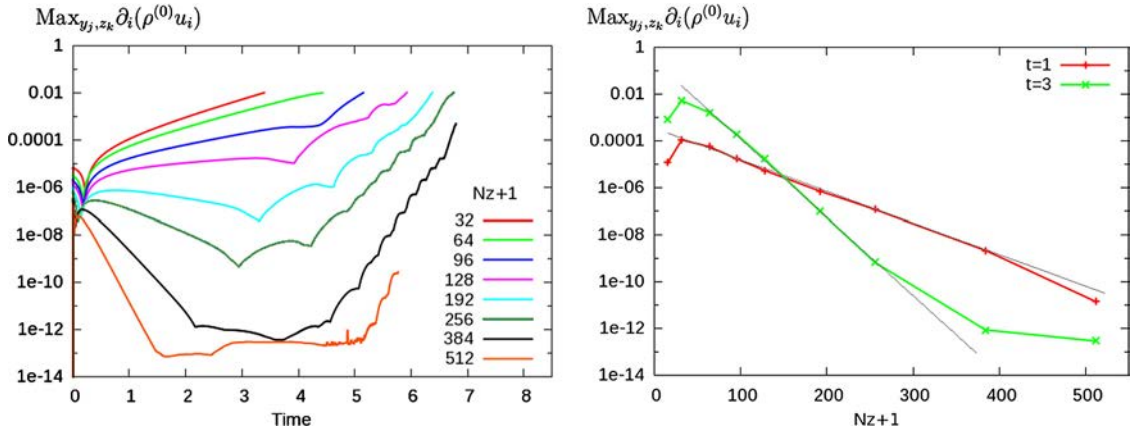

Fig. 5. Left: Evolution of $\text{Max}_{y_j,z_k}\partial_i(\rho^{(0)}u_i)$ versus time for the 8 simulations. The only varying parameter is the number of Chebyshev collocation points N_z. Right: $\text{Max}_{y_j,z_k}\partial_i(\rho^{(0)}u_i)$ versus $N_z + 1$ at times $t = 1$ and $t = 3$. Grey straight lines show exponential convergence.

modes, (k_x, k_y), whose amplitudes are chosen randomly within the annulus $k_{min} \leq \sqrt{k_x^2 + k_y^2} \leq k_{max}$. Single-mode leads to the development of a single mushroom-like structure, while multi-mode initialization generates a mixing layer. In both cases the velocity perturbations are localized around the mid-plane separating heavy and light fluid.

4.1. Grid convergence study

We consider here for the grid convergence study a set of eight 2D-anelastic simulations whose characteristics are gathered in Table 3, line GC. The simulations have run in a 2D-square domain, $(L_y = L_z \equiv 1)$, with one single domain discretized on a Gauss–Lobatto grid. Multi-mode initializations have been performed and the perturbations are located at $z = 0$. The linear regime ends approximately at time $t = 2.5$ and for $t > 4$, mushroom-like structures begin to develop. The number of Chebyshev collocation points varies from 32 to 512. The number of Fourier modes is high enough $(N_y = 1024)$ to ensure that the numerical errors are dominated by the Chebyshev discretization. Since $\partial_i(\rho^{(0)}u_i) = 0$ belongs to the system equations, the discrete momentum divergence maximum $\text{Max}_{y_j,z_k}\partial_i(\rho^{(0)}u_i)$ is taken as an indicator of the numerical error related to the spatial resolution. The left part of Fig. 5 shows that every increase in the number of collocation points causes an improvement of the accuracy. The $N_z + 1 = 512$ case exhibits a saturation of the maximum of the momentum divergence. The spatial average of the absolute value of the momentum divergence for the $N_z + 1 = 512$ case and for $2 \leq t \leq 5$ shows a saturation (graph not included) at a level close to the machine precision $(0.22204 \times 10^{-15})$. In the right part of Fig. 5,

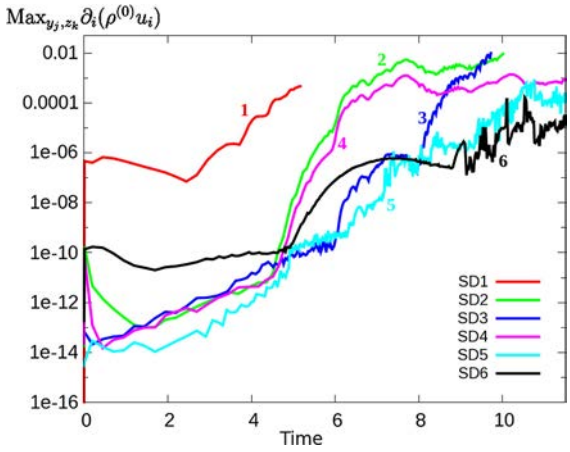

Fig. 6. Maximum of the divergence momentum, $\partial_i(\rho^{(0)}u_i)$, versus time. Results obtained from simulations SD1–SD6 (Table 4) are represented.

Table 4
Accuracy reached at the final time and computational performance of cases SD1–6. Every simulation has run on 128 cores. The first three simulations did not reach the final time, due to a stopping criterion on the momentum divergence.

Case	Vertical grid $N_d \times (N_z+1)$	Interface locations $z=$	Max$_{y_j,z_k}\partial_i(\rho^{(0)}u_i)$ (final time)	Average time step (10^{-4})	CPU time/cycle (s)	CPU time/unit of physical time (10^3 s)
SD1	1×512	no interf.	not reached	12.6	20.1	16.0
SD2	2×256	0	not reached	7.19	3.93	5.47
SD3	4×128	$-0.1; 0; 0.1$	not reached	3.28	0.938	2.84
SD4	4×128	$-0.25; 0; 0.25$	9×10^{-4}	4.38	0.914	2.08
SD5	4×128	mobile	2×10^{-4}	2.28	0.937	4.03
SD6	8×64	"	2×10^{-5}	3.10	0.595	1.89

the values of Max$_{y_j,z_k}\partial_i(\rho^{(0)}u_i)$ at time $t=1$ and $t=3$ are plotted versus N_z+1, in semi-log coordinates. The data clearly show an exponential convergence. The solution at time $t=1$ is stiffer than the one at $t=3$. As a result, convergence is slower but still exponential.

4.2. Optimal multidomain grid

We consider here a set of six 2D-anelastic simulations whose characteristics are gathered in Table 3, lines SD1 to SD6. These test cases share the same total number of collocation points. The aim here is to study the influence of the number of subdomains and the behavior of the auto-adaptive method. For a physical study, the grids would have been refined as soon as the accuracy became too low (Max$_{y_j,z_k}\partial_i(\rho^{(0)}u_i) \geq 10^{-7}$). The simulations have run in a rectangular 2D-domain, ($L_z=2$) and the same initialization than the simulation GC is used. The linear regime ends approximately at time $t=3$ and for $t>5$, mushroom-like structures begin to develop. A mixing layer appears at $t\approx8$. At final time $t=11.5$, the flow structures extend from $z\approx-0.25$ to $z\approx0.25$.

Results are shown in Fig. 6 and summarized in Table 4. Interfaces are fixed for simulations SD2–SD4. SD3 and SD4 share the same number of subdomains. While the SD3-interfaces are located near $z=0$, the SD4-interfaces are ideally located to capture the mixing layer at final time. Let us now comment the results. The single-domain simulation SD1 shows mediocre accuracy. Case SD2 is also inaccurate. Indeed it uses only two subdomains, and thus too few collocation points are located in the mixing layer. Gauss–Lobatto collocation point distribution emphasizes the borders of the domain, so that very few points are located near $z=0$. The SD3-case interfaces are located closer to $z=0$, the accuracy is good until time $t=8$. After that, as the structures of the flow go beyond the interfaces and enter the very large subdomains $[-1;-0.1]$ and $[0.1;1]$, the numerical errors rise sharply. The interfaces of case SD4 are well-located to capture the development of the mixing layer and the simulation is successful. Case SD5 shares the same grid as cases SD3 and SD4 but its interfaces are auto-adapted. It combines both good behaviors of fixed grids. On the one hand, the interfaces are located near $z=0$ at the beginning of the simulation, so that the accuracy is as good as simulation SD3 (actually slightly better). On the other hand, after $t=8$, the mixing layer is well calculated as the interfaces move away from each other, to follow the structures of the flow. Again, the accuracy is slightly better than the equivalent fixed interface case SD4. The last case is SD6. While this 8-subdomain simulation displays good accuracy during the linear growth, other cases do better. However, as soon as the mixing layer appears, the accuracy of case SD6 is better than the other ones. In the end, only three simulations reach the final time $t=11.5$, two with auto-adaptive grids and one with a fixed grid, where the interfaces have been manually and ideally placed.

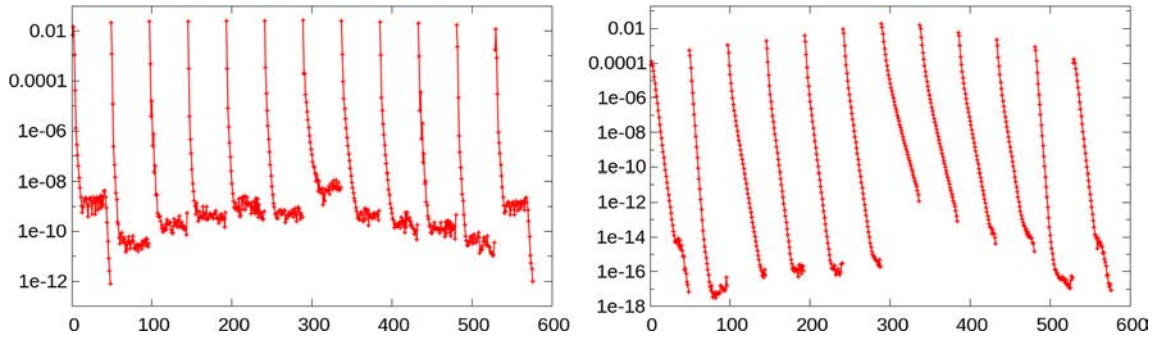

Fig. 7. Chebyshev spectra of pressure (left) and velocity u_z (right) from the simulation AM2 (Table 3). Grid is $[N_x, N_y, N_d \times (N_z+1)] = [600, 600, (12 \times 48)]$ and time is $t = 11.44$. Each graph shows 12 spectra, one per subdomain.

From results of Table 4, it may be concluded that:

- The 8-auto-adaptive-subdomain simulation SD6 improves the momentum-divergence, $\mathrm{Max}_{y_j,z_k}\partial_i(\rho^{(0)}u_i)$, by a factor 10 over the 4-auto-adaptive-subdomain simulation SD5, although they share the same number of collocation points.
- CPU time per time cycle greatly increases with the number of Chebyshev collocation points per subdomain.
- The average time steps of auto-adaptive simulations are rather small, because the interfaces keep being located as close to each other as possible during the linear growth of the RTI. As a consequence, while the 4-auto-adaptive-subdomain SD5 simulation displays the same CPU time per cycle as the 4-fixed-subdomain SD3 and SD4 simulations, its CPU time per unit of physical time is higher.
- The 8-auto-adaptive-subdomain simulation SD6 combines the best accuracy and the lowest computational cost.

In addition, the relationship between the grid size and the number of floating-operations needed may be estimated. Doubling the number of collocation points multiplies the number of floating-operations by 4 for the main parts of the numerical algorithm. The calculation of the Uzawa operator requires $(N_z+1)^3$ floating-operations but this remains negligible. On the other hand, doubling the number of subdomains only doubles the number of floating-operations. This explains the computational swiftness of the 8-subdomain simulation.

A simple argument explains why a 8-subdomain simulation shows better accuracy than a 4-subdomain simulation. The auto-adaptive algorithm always puts an interface on each bound of the mixing layer. This means that the first and the last subdomain of the grid are large. As both fluids may be considered at rest outside the mixing layer, these two subdomains are of a limited utility. The number of subdomains located inside the mixing layer is 2 for a 4-subdomain grid (50%), and 6 for a 8-subdomain grid (75%). More collocation points located around the gradients means better accuracy. More interfaces also means more degrees of freedom and thus the auto-adaptive algorithm is more efficient. However, too many subdomains may diminish the accuracy. Renaud and Gauthier [47] observed that the best Chebyshev derivation accuracy is obtained for $40 < N_z + 1 < 80$. Below 40, there are not enough polynomials to get a fine discretization. Above 80, numerical errors accumulate and cancel the benefit of additional modes. Let us recall that, through an interface, pressure is only C^0, velocity components u_1 and u_2 are C^1 and u_3 is C^2. As a result, the larger the number of interfaces, the larger the numerical errors.

As a conclusion, a recipe to determine the optimal number of subdomains could be the following

- For a small grid (for example, for reproducing the RT-linear growth), 30 collocation points per subdomain are enough, and at least 8 subdomains.
- As more collocation points are required, add subdomains then increase the number of collocation points per subdomain.
- When the number of collocation points per subdomain reaches 80, only add subdomains.

4.3. Pressure and velocity spectra

In order to check the behavior of the entire method, velocity and pressure Chebyshev spectra are displayed in Fig. 7. They are extracted from the anelastic simulation AM2 (Table 3) and are obtained by horizontal averaging. Six different grids were used for this simulation, i.e., five manual grid refinements were performed. At $t = 11.44$, the grid contains 12 subdomains with 48 Chebyshev collocation points, and 600 Fourier points in each horizontal direction. Every spectra displays an exponential decay of the Chebyshev coefficients. A saturation is observed in nearly all subdomains for the last Chebyshev modes. The level of Chebyshev coefficient saturation is related to the accuracy of the spatial discretization. The first and last subdomains are located outside the mixing layer and they are the largest subdomains: their accuracy is not as good as their nearest neighbors. In RT-induced mixing layers, smallest turbulent scales are located around $z = 0$. This explains that the saturation/accuracy is higher/worse for central subdomains. Subdomains 7 and 8 display a z-velocity spectra without saturation, it means that these subdomains may lack a small amount of collocation points.

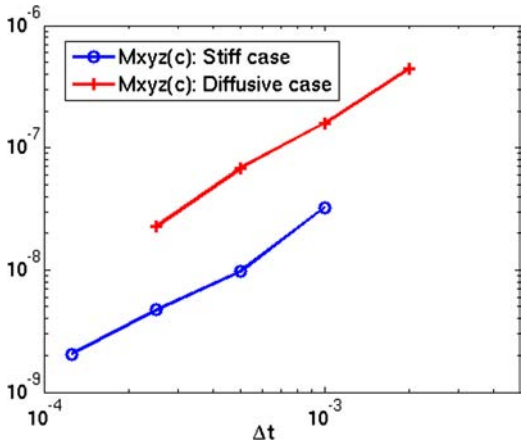

Fig. 8. Numerical errors defined by equation (72) for the mean value of the concentration $\bar{c}^{xyz}$, versus the time step Δt_n, in log–log scales. A linear fit gives a slope of 1.33 for the stiff simulation AL 1.33 and 1.43 for the diffusion solution AT.

4.4. Time step convergence

The temporal convergence is studied by means of the concentration average $\bar{c}^{xyz}$, computed at spectral accuracy. The Chebyshev quadrature is performed with the Clenshaw–Curtis formula [46] and the horizontal mean value is obtained from a Fourier-transform. Five runs of the simulation AL (Table 3) have been carried out with a fixed value of the time step, $\Delta t_n = \Delta t/n$, where $\Delta t = 10^{-3}$, with $n = 1, 2, 4, 8, 16$. A diffusion solution AT (Table 3) with a smoother initial density gradient and with no velocity, has also been studied. The parameters are $Sc = 0.7$, $Re = 10^3$. Five time steps have been used such that $\Delta t_n = \Delta t/n$, where $\Delta t = 10^{-3}$, with $n = 1/2, 1, 2, 4, 8$. The temporal errors are defined as

$$E^2_{AL,\,n} = \frac{1}{N}\sum_t [\bar{c}^{xyz}_n(t) - \bar{c}^{xyz}_{16}(t)]^2 \quad \text{for} \quad n = 1, 2, 4, 8, \text{ and}$$
$$E^2_{AT,\,n} = \frac{1}{N}\sum_t [\bar{c}^{xyz}_n(t) - \bar{c}^{xyz}_{8}(t)]^2 \quad \text{for} \quad n = 1/2, 1, 2, 4, \tag{72}$$

where N is the number of time samples. The error for both simulations is displayed in Fig. 8 as a function of the time step, in log–log scales. A linear fit gives a slope of 1.33 for the stiff simulation AL and 1.43 for the diffusion solution AT. These exponents are smaller than 2, the theoretical order of the Runge–Kutta scheme. They are however strictly larger than one. Several factors may affect this result. First there is no exact solution, only reference solutions calculated with $\Delta t/16$ or $\Delta t/8$. Numerical errors are usually dominated by spatial errors. This is also true in these cases, particularly for the stiff solution AL. Finally the iterative procedures run until the residual reaches 10^{-12}: a smaller time step results in less iterations. This prevents the simulations to totally benefit from the time step decreases.

4.5. Parallelization

4.5.1. Main features

The simulation code is parallelized on three different scales, two levels with MPI and the third one with OpenMP.

1. Each subdomain is dedicated to a group of MPI processes. Communications between two different groups of MPI processes mainly occur when matching calculations are performed.
2. Within a subdomain, each MPI process is in charge of a fraction of the $N_z + 1$ Chebyshev collocation points. Fourier derivatives are computed without communication, while Chebyshev derivatives need intense communications.
3. Each MPI process can be dedicated to several CPU cores through OpenMP.

A critical decision is whether to rely on a great number of MPI processes without OpenMP or a smaller number of MPI processes, each of them being parallelized with OpenMP. The former involves more communications between MPI processes. The entire calculation procedure is parallelized with MPI, whereas only some parts of the algorithm is parallelized with OpenMP. This distribution has to be calibrated to get the optimal performance.

4.5.2. Various benchmark results

We focus here on the anelastic simulation AM1 and measure diverse CPU times: CPU time per time cycle; CPU time per time cycle and per point; CPU time per core, per time cycle and per point. Results are summarized in Table 5. The simulation is started with a very small grid, which is later refined as RT-turbulence develops. Parallelization is defined by:

Table 5
Computational times (CPU time per time cycle; CPU time per time cycle and per point; CPU time per core, per time cycle and per point) for different grids and parallelization configurations. Parallelization is defined by: number of cores = number of subdomains × number of MPI processes per subdomain × number of OpenMP threads per MPI process.

Case	Grid $M \times (N_z+1) \times N_x \times N_y$	Parallelization $N_{cores} = M \times N_{MPI/d} \times N_{OpenMP/MPI}$	CPU time/time cycle (s)	CPU time/time cycle/point (μs)	CPU time/core/time cycle/point (ms)
AM1a	$16.8 \times 10^6 = (8 \times 32) \times 256^2$	$128 = 8 \times 16 \times 1$	13.2	0.789	0.101
AM1b	$56.6 \times 10^6 = (8 \times 48) \times 384^2$	$128 = 8 \times 16 \times 1$	44.2	0.781	0.100
AM1c	$70.8 \times 10^6 = (10 \times 48) \times 384^2$	$160 = 10 \times 16 \times 1$	49.7	0.708	0.112
AM1d	$207 \times 10^6 = (12 \times 48) \times 600^2$	$576 = 12 \times 48 \times 1$	50.9	0.246	0.142
AM1e	$207 \times 10^6 = (12 \times 48) \times 600^2$	$576 = 12 \times 24 \times 2$	61.0	0.294	0.169
AM1f	$207 \times 10^6 = (12 \times 48) \times 600^2$	$288 = 12 \times 24 \times 1$	79.8	0.385	0.111

number of cores = number of subdomains × number of MPI processes per subdomain × number of OpenMP threads per MPI process. Compared with case AM1a, the grid of case AM1b has been refined a little in each direction while keeping the same parallelization configuration. The global efficiency—evaluated by the calculation time per core, time cycle and collocation point—is unchanged. The measurements of case AM1c give a similar conclusion. A 17-million to 71-million grid point increase has only a slight impact on the efficiency. Let us comment on case AM1d. The number of MPI processes had to be increased, in order for the supercomputer memory to contain the bigger grid. More MPI processes implies more communications: the efficiency declines. Case AM1e has run on the same amount of cores than case AM1d and activates OpenMP along with a reduction of the number of MPI processes. MPI communications are faster as there are less MPI processes; however some parts of the numerical algorithm could not be parallelized with OpenMP. That is why case AM1e is 20% slower than case AM1d.

Case AM1f has run on twice as less cores than cases AM1d and AM1e. While the efficiency of cases AM1d and AM1e is lower, the efficiency of case AM1f is as good as the efficiency obtained with smaller grids (where the MPI communications are negligible).

- Comparison of the cases AM1f–AM1d: increasing the amount of MPI processes by a factor of 2 accelerates the calculation by 57%;
- Comparison of the cases AM1f–AM1e: increasing the amount of OpenMP threads by a factor of 2 accelerates the calculation by 30%.

From these example we can conclude that the two-level MPI parallelization is more efficient than the OpenMP parallelization of the code. While we prioritize the use of MPI over OpenMP, it is not possible to set more MPI processes per subdomain than the number of Chebyshev points in the subdomain. If the maximum number of MPI processes is not sufficient to handle the grid, in terms of memory usage, then one must use the memory associated with several cores for one MPI process. OpenMP parallelization is thus activated as it does not require more memory: this prevents the supercomputer to be under-used.

The code spends from 0.1% to 10% on the auto-adaptive algorithm, depending of the properties of the phenomena that is calculated. If it develops rapidly among the z-direction, many interface displacements have to be computed.

5. Algorithm and numerical code validation

5.1. Validation against the linear theory

The first step of the validation is given by a comparison of the linear growth stage of the anelastic-RTI with theoretical estimates. The 2D single-mode simulation AL (Table 3) has run with the following physical parameters: $At = 0.10$, $Re = 10^6$, $Sc = 10^3$, $Sr = 1$, $\gamma_{H,L} = 5/3$, $Pr = 0.7$, and the initial perturbation wave number is $k = 2\pi$. The Reynolds and Schmidt numbers are high enough to minimize momentum and concentration diffusion. Indeed the dimensionless coefficient of concentration diffusion is equal to 10^{-9}. Fig. 9 (left) shows the half width h of the perturbation amplitude versus time, given by the simulation. These data are fit, with $h_{th}(t) = h_0 + A\cosh\big(\sigma_{sim}(t - t_0)\big)$. Five fits are calculated, on the following time intervals: [0; 5.8], [1; 5.8], [2; 5.8], [3; 5.8] and [4; 5.8]. At $t = 5.8$ the linear stage is over as $hk = 0.314$. Indeed the classical criteria is $hk \ll 0.1$. The second fit is plotted versus time on the left (red line). On the other hand, three estimates of the linear growth rate are available. Duff et al. [18] provide the heuristic formula

$$\sigma_{DHH} = \sqrt{\frac{At\,k}{\psi} + \frac{k^4}{Re^2}} - \left(\frac{1}{Re} + \frac{1}{Sc\,Re}\right)k^2, \tag{73}$$

which takes into account viscosity and diffusion but not the stratification of the fluids. For $\psi = 1$, one obtains $\sigma_{DHH} = 0.793$. They also give the time-dependency of ψ. For $At = 0.1$, we measure the slope from Fig. 10 of Duff et al. [18] and one gets

$$\psi(t) = 1 + 0.833\,k\left(\frac{t}{Sc\,Re}\right)^{1/2}, \tag{74}$$

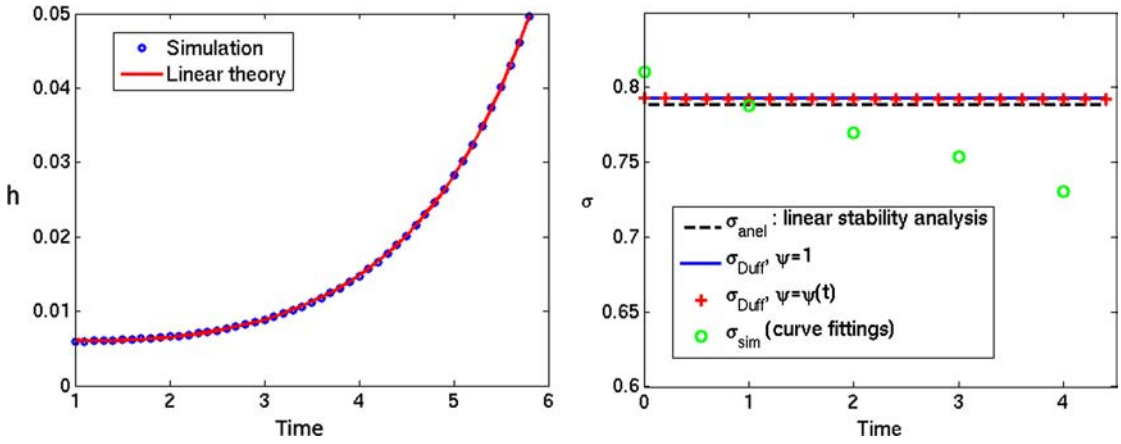

Fig. 9. Left: half width of the perturbation amplitude versus time during the linear growth regime for numerical simulation AL (blue dots). The numerical data are fit with $h_0 + A\cosh(\sigma_{sim}(t - t_0))$ (red line). Right: Values of the growth rates, obtained with: Duff et al. [18] formulas, anelastic linear stability analysis (Appendix C) and simulation results (five curve fits). (For interpretation of the references to color in this figure legend, the reader is referred to the web version of this article.)

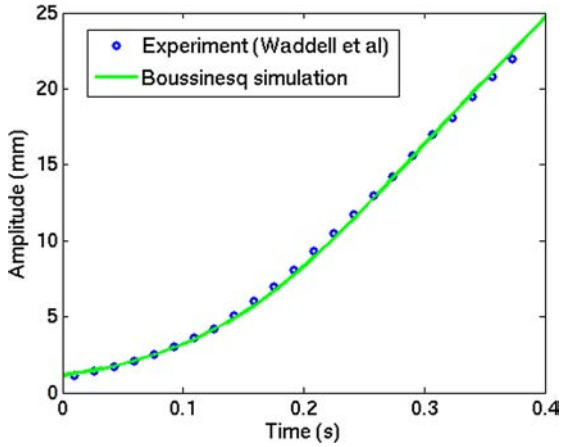

Fig. 10. Plot of measured amplitude versus time for the Waddell et al. [55] experiment (Fig. 8) (blue dots), and for the simulation BW (green line). (For interpretation of the references to color in this figure legend, the reader is referred to the web version of this article.)

which is plotted on the right part of Fig. 9 with red crosses. It does not visually differ from the case $\psi =$ constant, plotted with a blue line. Finally the linear stability analysis for perfect fluids carried out on the anelastic equations (6)–(10) provides the theoretical anelastic growth rate in presence of stratification $\sigma_{th} = 0.7885$ (Appendix C). It is also plotted in Fig. 9 with a dashed black line. These three theoretical estimates give very similar results. Indeed the Reynolds and Schmidt numbers are fairly high and the stratification parameter is low, so that these values are very close the RT-classical growth rate, $\sqrt{At\,k}$, valid for perfect incompressible fluids in an infinite geometry. The growth rate values calculated from the simulation are displayed with green dots, on the right part of Fig. 9. These values are slightly decreasing as fitting focus more and more on the end of the linear growth regime, where the gradients have been smoothed by the fluid motion.

5.2. Validation against the Waddell et al. [55] single-mode experiment

Waddell et al. [55] carried out several RTI experiments. They consider low Atwood number liquid systems. Two different Atwood numbers have been used, $At = 0.155$ and 0.336. The latter is too high for the Boussinesq model (compressibility effects probably occur), so we choose the former for this validation study. As there is no stratification in these experiments, the anelastic model cannot be used. The acceleration is $0.74\,g$, with an initial perturbation wavelength of $L_y = 54$ mm which is taken as the reference length for the calculation of dimensionless numbers. The calcium nitrate solution is considered as saturated, so that the diffusion coefficient is $\mathcal{D} = 10^{-9}\ \mathrm{m^2\,s^{-1}}$ and the dynamic viscosity coefficient is chosen to be $\mu = 7 \times 10^{-3}\ \mathrm{N\,s\,m^{-2}}$. The simulation BW (Table 3) is characterized by $Re = 4.97 \times 10^3$, $Sc = 6.797 \times 10^3$ and is seeded with a single-mode perturbation. Fig. 10 displays the perturbation amplitude obtained from this simulation versus time (green line), which is in excellent agreement with the experimental data represented with blue dots. The dimensionless time of the simulation is t_{sim}, its corresponding real time (in seconds) is

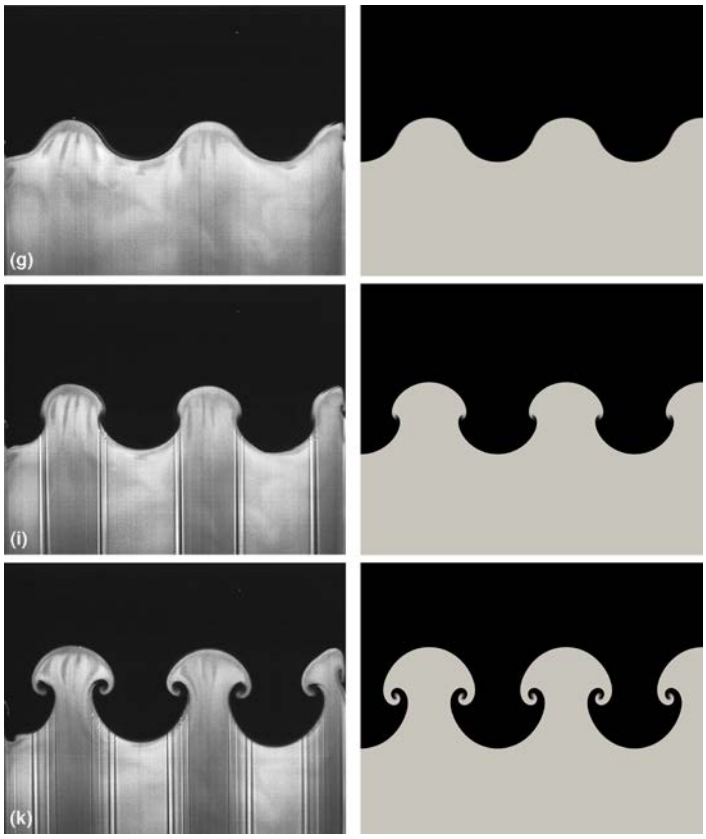

Fig. 11. Left column: Sequence of images extracted from Waddell et al. [55] (figure 4) showing the growth of a single-mode RTI. The time increment between each image is 0.033 s. Right column: Sequence of images obtained from the simulation BW showing the growth of the same instability. Note that each frame is composed of twice and the half of the same image, this duplication has been made for visualization purpose.

$$t_{sim}^{dim} = t_{sim}\sqrt{L_y/g} - \delta t, \tag{75}$$

where $\delta t \approx 0.14$ s is the time lap between chronologies of the simulation and the experiment. A sequence of images showing the development of the instability is extracted from Waddell et al. [55] and displayed in Fig. 11, left column. The corresponding simulation results are presented in the right column. As the Atwood number is $At = 0.155$, there is a slight width difference for the mushroom-like structures observed in the experiment. Those composed of light fluid are a bit narrower than the heavy fluid ones (see image (k) in Fig. 11). This Atwood number effect is not taken into account by the Boussinesq model. Thus, bubble and spike widths are identical in the simulation. Aside from this, experiment and simulation results match very well.

In Fig. 12, 2D map of concentration is represented and the 15-interfaces have been made visible. Subdomains are gathered in three spots, first at the front of the spike, second at the rolling between the spike and the bubble and third at the top of the bubble. As vertical gradients are steeper at these locations, the auto-adaptive algorithm places more subdomains. The right part of Fig. 12 shows the evolution of the interface locations versus time. They move away from each other to follow the growing structure. It is worth noting that the upper interface behavior is quite oscillating up to $t \approx 6.7$, where the upper subdomain becomes necessary to describe the solution.

5.3. Calculation of the α_b-coefficient in a turbulent RT-mixing layer

It is well-known that Boussinesq RT-mixing layers follow a self-similar law such as $h_b \sim \alpha_b\, At\, g\, t^2$, where h_b is the bubble (or spike) height and α_b is a constant [57]. The value of α_b has been the object of large debates over the last decades. The consensus is now that values of α_b are between 0.020 and 0.030 for miscible fluids [25,57], provided that turbulence has been seeded by small wavelength perturbations. As a global validation of the method, we use the data of a large-scale Boussinesq simulation, referenced line BM, Table 3. From these data, the coefficient α_b is calculated in two ways. First, if the transition to a self-similar state is achieved at time $t = t_o$, the scaling law actually writes

$$h(t) = h_o + \alpha_{b1}\, At\, g\, (t - t_o)^2 \quad \text{or} \quad \frac{\dot{h}}{2\, At\, g\, t} = \alpha_{b1}\left(1 - \frac{t_o}{t}\right). \tag{76}$$

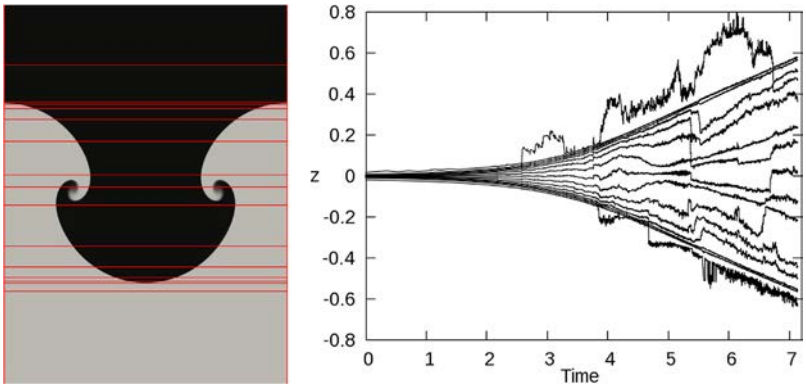

Fig. 12. Left: 2D map of concentration obtained from the simulation BW showing the 15-interface locations at time $t = 5.2$. Right: Location of these interfaces versus time.

It is also possible to fit the numerical data with a second order polynomial, as $h(t) = p_0 + p_1 t + p_2 t^2$. The expression of the α_{b2}-coefficient is therefore

$$\alpha_{b2} = \frac{p_2}{At\, g}. \tag{77}$$

The first method gives a time-dependent value such that $0.020 < \alpha_{b1} < 0.023$. The second way leads to $\alpha_{b2} = 0.021$, for a fit performed in the time interval $9 < t < 15.7$. Both values are in good agreement with the consensus.

6. Simulation results

As an illustration of the numerical method detailed above, four 3D simulations have been carried out, three with the anelastic model (AS, AM1 and AM2) and one with the Boussinesq approximation (BM). Let us recall that the initial equilibrium state is described in Section 2.2. The horizontal size of the computational domain is 1×1. Different heights are used in the four simulations.

6.1. Single- and multi-mode anelastic simulations

The first anelastic simulation (line AS, Table 3) is initialized with a single-mode velocity perturbation. Parameters are $Sr = 0.20$, $At = 0.20$, $Re = 5 \times 10^3$, $Sc = 0.71$, $Pr = 0.71$ and $\gamma = 5/3$ for both fluids. The vertical size of the domain is $[-1.3, 1.2]$. The grid is composed of 10 subdomains, each with 64 Chebyshev collocation points, and 384^2 Fourier modes. Fig. 13 displays an isosurface of vorticity colored by the concentration in heavy fluid (left), which has a torus shape. On the right, the isosurface of concentration is colored by the velocity divergence and displays a mushroom-like structure. The local Mach number grows quickly with time and reaches $Ma = 0.504$ ($\gamma\, Ma^2 = 0.427$) at the core of the mushroom. This is a limit value for the anelastic approximation.

The second anelastic simulation (line AM1, Table 3) is initialized with a multi-mode velocity perturbation whose Fourier modes are chosen randomly within an annulus defined by $k_{min} = 138.2$ and $k_{max} = 169.6$. It uses the following set of parameter values: $Sr = 2$, $At = 0.25$, $Re = 10^4$, $Sc = 0.7$, $Pr = 0.7$ and $\gamma = 5/3$ for both fluids. The vertical computational domain is $[-0.5{:}{+}0.5]$. Spatial resolution is increased as turbulence develops and more and more modes are involved. The simulation is started with 8 subdomains with 32 Chebyshev collocation points in each one and with 256^2 Fourier modes. The grid is set to $(8 \times 48) \times 384^2$ at $t = 3$, $(10 \times 48) \times 384^2$ at $t = 4.47$ and finally $(12 \times 48) \times 600^2$ at $t = 5.54$. The calculation has been stopped at $t = 9.3$ when the mixing layer reaches the top of the domain. Fig. 14 displays the vorticity isosurface colored by the concentration (left), and the two isosurfaces of concentration, $c = 0.05$ and $c = 0.95$ (right) colored by the velocity field divergence. The isosurfaces of concentration clearly reveal large scale bubbles on the top and the velocity divergence reaches its maximal values inside the mixing layer. The vorticity isosurface shows the chaotic character of the flow. Fig. 15 (left) displays the evolution of the subdomain interface locations versus time. At times $t = 4.47$ and $t = 5.54$ two subdomains have been added to follow the complexity of the flow. The right part of Fig. 15 displays the evolution of the norm of the test function. As the mixing layer develops, density and concentration gradients smooth, therefore the norm of the test function decreases and so do the numerical errors. At late times, there are some interactions between the mixing layer and the upper boundary of the domain. Fig. 14 shows clearly these interactions on the large-scale bubbles.

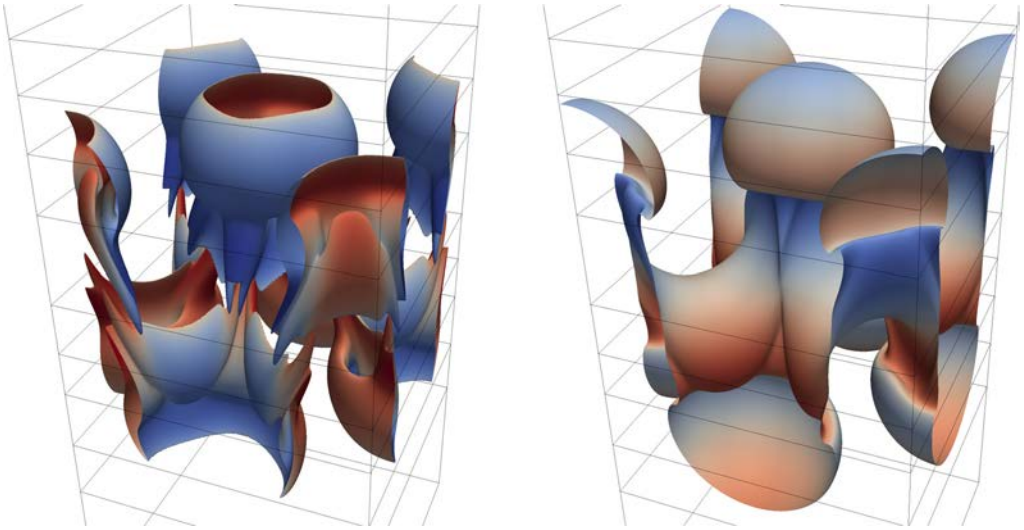

Fig. 13. Simulation AS. RT single-mode simulation carried out with the anelastic model for the following set of parameter values: stratification $Sr = 0.2$, Atwood $At = 0.2$, Reynolds $Re = 5 \times 10^3$, Schmidt $Sc = 0.71$, Prandtl $Pr = 0.71$ and $\gamma = 5/3$. The vertical size of the computational domain is $[-1.3{:}{+}1.2]$ and the spatial resolution is $(10 \times 64) \times 384^2$. A mushroom-like structure develops and it is presented from the bottom in order to have a full view on the vorticity torus. As the Atwood number is low, the flow displays a particular vertical symmetry. Left: vorticity isosurface $|\omega| = 7$ colored by the concentration (low values in blue and large values in red). Right: isosurface of concentration $c = 0.5$ colored by the velocity field divergence, $-1.13 \times 10^{-1} \leq \partial_i u_i \leq 9.77 \times 10^{-2}$. Horizontal black lines are the subdomains interfaces. Time is 5.9, 14,099 time cycles and 51 collocation point distribution adaptations were carried out. (For interpretation of the references to color in this figure, the reader is referred to the web version of this article.)

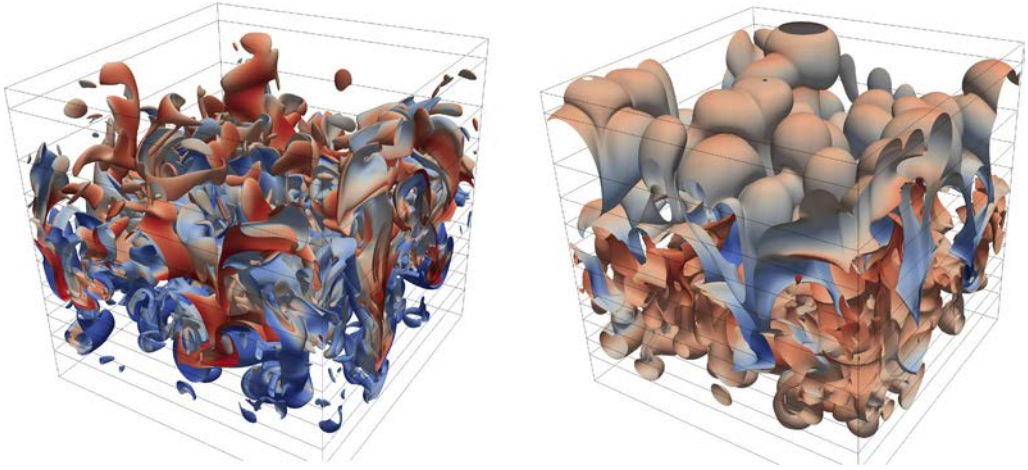

Fig. 14. Simulation AM1. RT mixing layer simulation carried out with the anelastic model. The set of parameter values is: stratification $Sr = 2$, Atwood $At = 0.25$, Reynolds $Re = 10^4$, Schmidt $Sc = 0.7$, Prandtl $Pr = 0.7$ and $\gamma = 5/3$. The vertical size of the computational domain is $[-0.5{:}{+}0.5]$ and the spatial resolution is $12 \times 48 \times 600^2$. The mixing layer develops, progressively fills out the domain and reaches the top boundary. Left: vorticity isosurface colored by the concentration. Right: isosurfaces of concentration $c = 0.05$ and $c = 0.95$, colored by the velocity field divergence, $-0.89 \leq \partial_i u_i \leq 0.71$. Horizontal black lines are subdomains interfaces. Time is 9.3, 15,520 time cycles and 174 collocation point distribution adaptations were carried out. (For interpretation of the references to color in this figure, the reader is referred to the web version of this article.)

6.2. Comparison between anelastic and Boussinesq turbulent RT-mixing layer

As already said before, the Boussinesq model is the simplest physical model for the RTI. Indeed the sole Kovásznay mode contained in this model is the vorticity mode. Neither static nor dynamic compressibility is present. Both fluids remain isothermal as there is no energy equation. Physical parameters for Boussinesq simulations are *At*, *Re*, *Sc* and the wave numbers describing the initial perturbation. Several extra physical parameters take part in anelastic simulations. First, the stratification parameter *Sr*, which is related to static compressibility. The anelastic model is valid for $Sr = \mathcal{O}(1)$, while in Boussinesq model there is no stratification, $Sr = 0$. Second, the adiabatic indexes $\gamma_{H,L}$, which are related to dynamic compressibility and energy equation. They are considered as infinite in the Boussinesq model. Third, the Prandtl number *Pr*, which is also related to the energy equation.

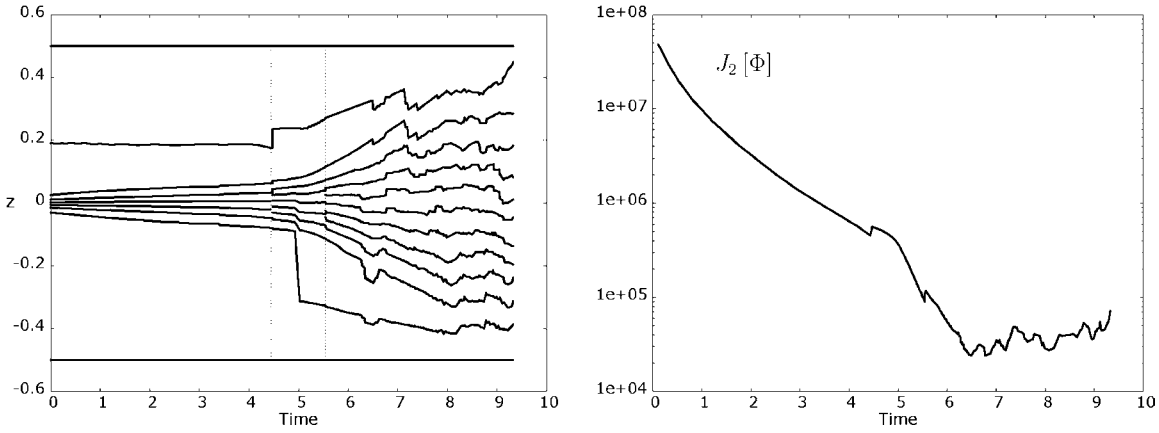

Fig. 15. Simulation AM1. Left: evolution of the subdomain interface locations versus time. At times $t = 4.47$ and $t = 5.54$ the increase of the number of subdomains are visible (see vertical dashed lines). Right: norm of the test function used in the auto-adaptive algorithm versus time. Recall that this norm bounds the numerical errors. The norm decreases as the main gradients (density and concentration) decrease. From $t \approx 7.5$ the mixing fills the domain and the norm oscillates at a low value.

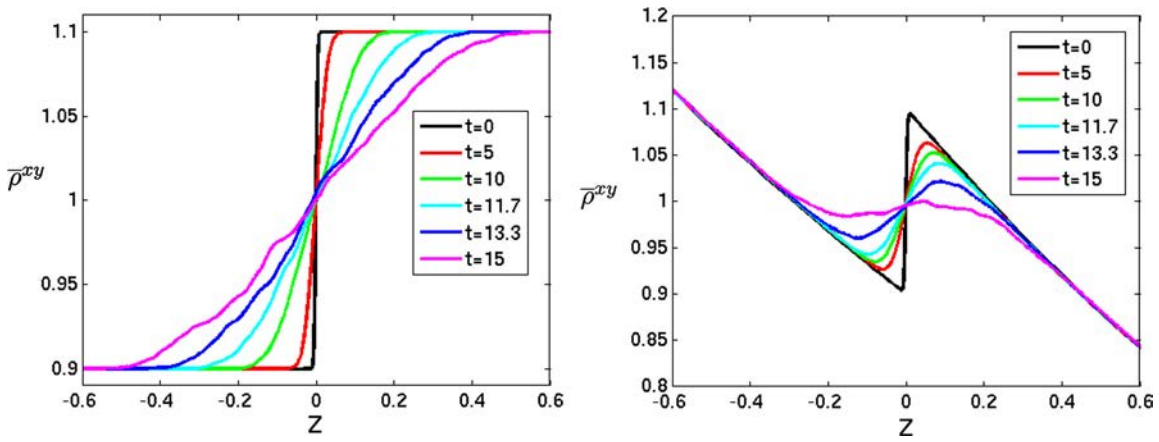

Fig. 16. z-profiles of the horizontal average density $\overline{\rho}^{xy}$. Left: Boussinesq simulation BM. Right: anelastic simulation AM2.

In this section we compare the results obtained from simulations AM2 (anelastic model) and BM (Boussinesq model), referenced in Table 3. This comparison is only sketched out here since a detailed study is out of the scope of this paper. Common physical parameters were set to same values, i.e., $At = 0.10$, $Re = 3 \times 10^3$, $Sc = 0.7$ and initial perturbations wave numbers $151 \leq k \leq 182$. Concerning Sr, $\gamma_{H,L}$ and Pr for the anelastic simulation, we could choose weak values for Sr and Pr, and extreme values for $\gamma_{H,L}$. This choice would cancel every additional physics contained in the anelastic model. However, aside from numerical difficulties induced by this choice, anelastic model is invalid for $Sr \ll 1$. We chose instead to run two similar but not identical simulations. In the anelastic one, stratification is weak but not negligible, $Sr = 0.4$, $\gamma_{H,L} = 5/3$ and $Pr = 0.7$ (common values for gases). This way, one can measure the importance of several physical phenomena on the growth of the RTI: static, dynamic compressibility and temperature effects. The initializations are as close as possible, the velocity perturbation satisfies the constraint equation $\partial_i u_i = 0$ for the Boussinesq simulation while it satisfies $\partial_i(\rho^{(0)} u_i) = 0$ for the anelastic one. Another way to describe the differences between Boussinesq and anelastic models is to think that Boussinesq approach deals with unstratified isothermal liquids while anelastic approximation deals with stratified gases. Both simulations BM and AM2 start with a small grid that is refined as turbulence develops. The anelastic simulation ends with $[N_x, N_y, N_d \times (N_z + 1)] = [816, 816, (30 \times 48)]$ and the Boussinesq simulation with $[940, 940, (24 \times 40)]$. The first result makes the difference more clear (see Fig. 16). The initial state differs. Indeed fluids has a constant density in the Boussinesq case while they are stratified in the anelastic model. Boussinesq mixing layer growth is potentially infinite since a self-similar state is reached (see Section 5.3). On the other hand, anelastic mixing layer growth is necessarily bounded, because after some time the density jump is erased. Then the turbulence and the anisotropy go to zero. Fig. 17 compares the development of the Boussinesq and anelastic simulations. The transient regime seems shorter for the Boussinesq case, as the mixing layer starts to widen sooner. Indeed the density jump in the anelastic configuration is smoothed by the instability process [24]. Right part of Fig. 17 displays the total kinetic energy for the two simulations. While the anelastic kinetic energy is a bit higher during the linear growth stage, it then stays weaker than the Boussinesq kinetic energy. After the turbulence regime has started, the anelastic kinetic energy bridges the gap and slightly exceeds the Boussinesq kinetic

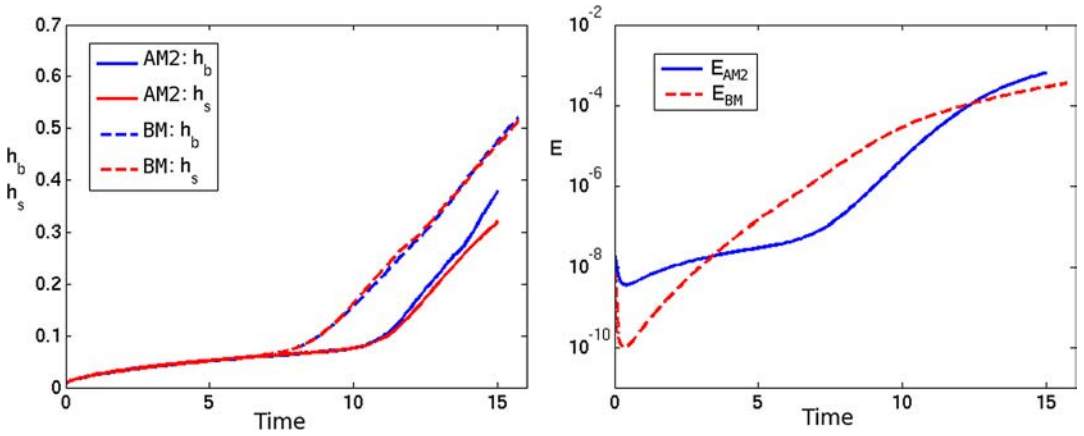

Fig. 17. Left: half-widths of the mixing layers for the simulations AM2 and BM. The bubble and spike thicknesses are h_b and h_s, respectively. The Boussinesq half-widths are equal since the flow is symmetric. Right: time evolution of the kinetic energy, $E_{BM} = 1/2\ \overline{u_i\, u_i}^{xyz}$ and $E_{AM2} = 1/2\ \overline{\rho\, u_i\, u_i}^{xyz}$.

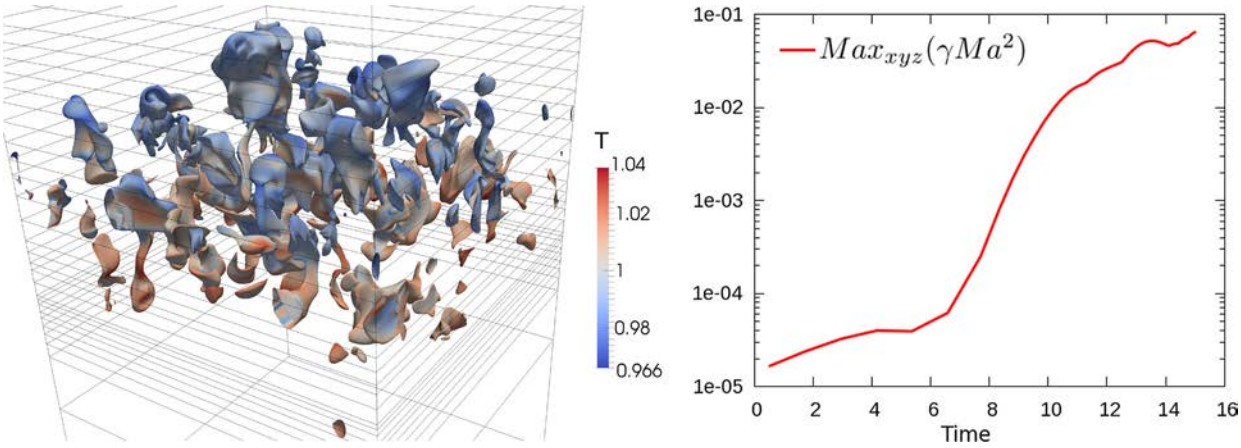

Fig. 18. Simulation AM2. Left: isosurface of Mach number $Ma = 0.1$ colored by the temperature, final time of the simulation. Right: Time evolution of spatial maximum $\mathrm{Max}_{xyz}(\gamma Ma^2)$. (For interpretation of the references to color in this figure, the reader is referred to the web version of this article.)

energy. Finally, Fig. 18 highlights compressible phenomena. On the left an isosurface of Mach number is displayed, colored by the temperature. Mach is low enough for the anelastic model to remain valid. The temperature varies from 0.96 to 1.04, where the temperature of the resting state is $T = 1$. Right part of Fig. 18 presents the evolution of γMa^2 versus time, this is a measurement of compressibility effects. Let us recall that the anelastic model is valid for γMa^2 much smaller than one, which is the case here. This quantity strongly increases during the establishment of the mixing layer, and slowly grows during the turbulence stage.

7. Conclusion

We have presented a consistent Chebyshev–Fourier–Fourier pseudo-spectral method for determining the numerical solution of anelastic models. The velocity field u satisfies the constraint $\partial_i(\widetilde{\rho}(z)\, u_i) = 0$, where $\widetilde{\rho}(z)$ is a mean density profile. In the particular application of the Rayleigh–Taylor instability for two miscible fluids—as studied in this paper—the final density profile obtained after the overturn of the two fluids has been used as the mean density $\widetilde{\rho}$. It has been previously shown that the associated anelastic Stokes problem is elliptic [30]. We have generalized the Uzawa decoupling method taking advantage of the horizontal periodicity of the flow. The Uzawa pressure operator properties have been detailed and the condition number of the pressure Uzawa operator was shown to behave closely to N_z^4. In the special case of the zero wave number $k = 0$, the solution was obtained with the $k = 0$—Uzawa pressure operator. The use of this operator lead to a more accurate result than that provided by the analytical solution. We solve the linear systems and refine the solutions using iterative algorithms. Time marching is handled in the Fourier space with a second-order three-step semi-implicit low-storage Runge–Kutta scheme, while the first time cycle is computed with a first-order scheme. This method is coupled with an auto-adaptive multidomain method that allows us to handle stiff situations. The matching of quantities between the subdomains is carried out with the influence matrix method. The entire algorithm is also reduced to the Boussinesq approximation. We have shown that the spectral accuracy is achieved. We have confirmed that a Chebyshev cut-off around

of 50 or 60—along with the associated number of automatically adapted subdomains—leads to the optimal accuracy and the lowest computational cost.

Temporal convergence has also been studied and was found to approach the second-order accuracy. Indeed, when the spatial errors are minimized—as is the case for a smooth diffusion solution—results are closer to their theoretical value. The linear growth rate of the anelastic approximation has been validated against those obtained from the heuristic model of Duff et al. [18], and by solving the anelastic linear eigenvalue problem. The algorithm for the Boussinesq approximation and the numerical code have been validated against the laminar single-mode experiment of Waddell et al. [55]. The nonlinear growth rate α_b of a turbulent RT-mixing layer has been computed and was found close to $\alpha_b = 0.021$. Both results are in good agreement with experimental data.

The anelastic and Boussinesq approximations have been compared using similar physical parameters. Relative to the Boussinesq simulation, the anelastic results exhibit a time delay for the transition to turbulence. Contrary to the Boussinesq model, the asymmetry between spikes and bubbles is observed in the anelastic simulation. The characteristics and computational performance of the resulting numerical code were analyzed. Finally several 3D anelastic and Boussinesq simulations have been carried out to (i) illustrate the capability of the complete algorithm to handle stiff problems, and (ii) describe the turbulent regime when starting from a resting state.

The combination of algorithms developed for these studies may be used in a large number of anelastic-type models, and remains accurate in the case of time-evolving steep gradients.

Acknowledgements

We wish to thank J.-M. Clarisse (CEA, DAM, DIF, Bruyères-le-Châtel) for useful discussions and in particular, for having pointed out the counterexample in Richtmyer and Morton [48]. This work was granted access to the HPC resources of TGCC under the allocation 2013-t20132a6133 made by GENCI.

Appendix A. Source term boundary conditions

The Uzawa method solves the velocity equations in the interior domain. As a result, source terms due to the boundary conditions appear in equations (36), (39), (41) and (43). To show this, we first notice that if (X_p) is a vector with $(N_z + 1)$ components, then $X'_p = \sum_{j=0}^{N_z} D_{pj} X_j$. Therefore

$$X'_{p,I} = X'_p - D_{p0} X_0 - D_{pN_z} X_{N_z}, \qquad p = 1, \ldots, N_z - 1. \tag{A.1}$$

This remark applies to the source terms appearing in equation (36), $\widetilde{\Sigma}_{u,k}^{(q)(s)}$ and $\widetilde{\Sigma}_{w,k}^{(q)(s)}$, which are expressed with the boundary conditions (33), and are a consequence of relation (A.1)

$$\begin{aligned}
\left[\widetilde{\Sigma}_{v,k}^{(q)(s)}\right]_p &= \left(D^2_{p+1,\,0}\,\delta_{1s} + D^2_{p+1,\,N_z}\,\delta_{2s}\right)/Re,\\
\left[\widetilde{\Sigma}_{w,k}^{(q)(s)}\right]_p &= \left(D^2_{p+1,\,0}\,\delta_{3s} + D^2_{p+1,\,N_z}\,\delta_{4s}\right)/Re\\
&\quad - {L_\rho^{-1}}_{\,p+1}(D_{p+1,\,0}\,\delta_{3s} + D_{p+1,\,N_z}\,\delta_{4s})/(3Re),
\end{aligned} \tag{A.2}$$

for $p = 0, \ldots, N_z - 2$. In the same way, the expression of the source term $\widetilde{\Sigma}_{v,k}^{\perp(q)(s)}$, which appears in equation (39) for $\widetilde{V}_{k,I}^{\perp(q+1)(s)}$, is

$$\left[\widetilde{\Sigma}_{v,k}^{\perp(q)(s)}\right]_p = \left(D^2_{p+1,\,0}\,\delta_{1s} + D^2_{p+1,\,N_z}\,\delta_{2s}\right)/Re. \tag{A.3}$$

Similarly, the additional source terms $\Sigma_{Dw}^{(q)(s)}$ and $\Sigma_{vw}^{(q)(s)}$ appearing in equation (41), are column vectors, which read

$$\begin{aligned}
\left[\Sigma_{Dw}^{(q)(s)}\right]_p &= D^2_{p+1,\,0}\,\delta_{3s} + D^2_{p+1,\,N_z}\,\delta_{4s}, \qquad p = 0, \ldots, N_z,\\
\left[\Sigma_{vw}^{(q)(s)}\right]_0 &= -k\,\delta_{1s} - {L_\rho^{-1}}_{\,0}\,\delta_{3s},\\
\left[\Sigma_{vw}^{(q)(s)}\right]_p &= 0, \qquad p = 1, \ldots, N_z - 1,\\
\left[\Sigma_{vw}^{(q)(s)}\right]_{N_z} &= -k\,\delta_{2s} - {L_\rho^{-1}}_{\,N_z}\,\delta_{4s}.
\end{aligned} \tag{A.4}$$

Appendix B. First time cycle

Semi-implicit time marching schemes require quantities at sub-cycle (q) to obtain quantities at sub-cycle $(q+1)$. In particular this means the pressure has to be initialized with a first-order temporal scheme at the beginning of the simulation. We use a semi-implicit Adams–Bashforth/backward differentiation scheme reduced to first-order ([46], Section 4.4). The momentum equation (24) discretized with this scheme writes

$$\frac{3u_i^{q+1} - 4u_i^q + u_i^{q-1}}{2\,\Delta t} = 2\,F_i^q - F_i^{q-1} + G_i^{q+1}, \qquad i = 1, 2, 3 \tag{B.1}$$

where F_i^q is the explicit term and G_i^q is the implicit term

$$\begin{aligned} F_i^q &= -u_j^q \partial_j u_i^q - \frac{1}{\rho^{(0)}} f_i^q, \\ G_i^q &= -\frac{1}{\rho^{(0)}} \left(\frac{1}{Sr} \partial_i + \frac{\rho^{(0)}}{p^{(0)}} \delta_{i3} \right) p^q + \frac{1}{\rho^{(0)} Re} \left(\partial_{jj}^2 u_i^q - \frac{1}{3} \partial_i (L_\rho^{-1} u_3^q) \right). \end{aligned} \tag{B.2}$$

This scheme is considered with $q = 0$ and $u^{-1} = u^0$, so that equation (B.1) writes

$$\frac{3}{2}\,\frac{u_i^1 - u_i^0}{\Delta t} = F_i^0 + G_i^1, \qquad \text{with } \partial_i(\rho^{(0)} u_i^1) = 0. \tag{B.3}$$

This is a first order temporal scheme in which the pressure at time cycle 0 no longer appears. This leads to a pressure field p^1, consistent with the velocity field u_i^1. To achieve good accuracy the time step is set to be one order of magnitude smaller than the time step associated with the Runge–Kutta scheme (see Section 3.8.1). In subsequent time cycles, the time step automatically grows until it reaches the value given by the stability criteria (69).

Appendix C. Linear normal mode analysis for perfect fluids

The linear stability analysis is carried out on the anelastic model defined by equations (6)–(10) in the limit of infinite Reynolds number. To this end, the model equations are first linearized and solutions are sought under the form

$$\phi(x, y, z, t) = \widehat{\phi}(z)\, e^{\sigma\, t}\, e^{\mathrm{i}\,(k_x x + k_y\, y)}. \tag{C.1}$$

We also assume that the flow is irrotational so that the velocity derived from a potential, denoted φ. From the constraint $\partial_i(\rho^{(0)}\, u_i) = 0$, one obtains the following ODE for the structure function $\widehat{\varphi}(z)$

$$d_{zz}^2 \widehat{\varphi} + {\rho^{(0)}}^{-1} d_z \rho^{(0)}\, d_z \widehat{\varphi} - (k_x^2 + k_y^2)\, \widehat{\varphi} = 0 \quad \text{or} \quad d_{zz}^2 \widehat{\varphi} - \mathcal{S}\, d_z \widehat{\varphi} - k^2\, \widehat{\varphi} = 0. \tag{C.2}$$

The boundary conditions associated to $\widehat{\varphi}$ are actually defined on the vertical velocity component $u_3 = d_z \widehat{\varphi}$. Indeed we assume Dirichlet boundary conditions at the top and the bottom

$$u_3(x, y, z = z_t, t) = u_3(x, y, z = z_b, t) = 0, \tag{C.3}$$

and continuity of the vertical velocity at the interface

$$\begin{aligned} u_3(x, y, z = 0^+, t) &\equiv u_{H3}(x, y, z = 0^+, t) = \dot{\xi}(0) = \sigma\, \xi(0), \\ u_3(x, y, z = 0^-, t) &\equiv u_{L3}(x, y, z = 0^-, t) = \dot{\xi}(0) = \sigma\, \xi(0). \end{aligned} \tag{C.4}$$

Solution of equation (C.2) is

$$\widehat{\varphi}_{H,L} = \lambda_{H,L}\, e^{r_1\, z} + \mu_{H,L}\, e^{r_2\, z} \tag{C.5}$$

with $r_{1,2} = (\mathcal{S} \pm (\mathcal{S}^2 + 4k^2)^{1/2})/2$. The boundary conditions (C.3) give the coefficients λ_{HL} in terms of the μ_{HL}'s. The Bernoulli equation

$$\rho_H(0)\, (\partial_t \varphi_H(0) + \xi(0)) = \rho_L(0)\, (\partial_t \varphi_L(0) + \xi(0)), \tag{C.6}$$

and the boundary conditions (C.4) give the relation of dispersion. We obtain

$$\sigma^2 = \frac{2\, r_2\, At}{(1 - At) F_L - (1 + At) F_H} \quad \text{with} \quad F_{HL} = \frac{1 - r_2/r_1 e^{-(r_2 - r_1) z_{bt}}}{1 - e^{-(r_2 - r_1) z_{bt}}} \tag{C.7}$$

References

[1] S. Abarzhi, S. Gauthier, K. Sreenivasan, Turbulent mixing and beyond: non-equilibrium processes from atomistic to astrophysical scales II, introduction, Philos. Trans. R. Soc. A 371 (2003) (2013) 20130268 (7 pp.).
[2] K. Arrow, L. Hurwicz, H. Uzawa, Studies in Nonlinear Programming, Stanford University Press, Stanford, 1968.
[3] P. Bannon, P. Chagnon, R. James, Mass conservation and the anelastic approximation, Mon. Weather Rev. 134 (2006) 2989–3005.
[4] J. Barranco, P. Marcus, A 3D spectral anelastic hydrodynamic code for shearing, stratified flows, J. Comput. Phys. 219 (2006) 353–365.
[5] A. Batoul, H. Khallouf, G. Labrosse, Une méthode de résolution directe (pseudo-spectrale) du problème de Stokes 2D/3D instationnaire. Application à la cavité entrainée carrée, C. R. Acad. Sci. Paris, Sér. II 319 (1994) 1455–1461.
[6] A. Bayliss, B. Matkowsky, Fronts, relaxation oscillations and period doubling in solid fuel combustion, J. Comput. Phys. 71 (1987) 147–168.
[7] J. Bell, M. Day, C. Rendleman, S. Woosley, M. Zingale, Adaptive low Mach number simulations of nuclear flame microphysics, J. Comput. Phys. 195 (2004) 677–694.
[8] G. Boffetta, A. Mazzino, S. Musacchio, L. Vozella, Statistics of mixing in three-dimensional Rayleigh–Taylor turbulence at low Atwood number and Prandtl number one, Phys. Fluids 25 (2010), 085107-17.
[9] C. Boudesocque-Dubois, J.-M. Clarisse, S. Gauthier, A spectral Chebyshev method for linear stability analysis of one-dimensional exact solutions of gas dynamics, J. Comput. Phys. 184 (2003) 592–618.
[10] W. Cabot, Comparison of two- and three-dimensional simulations of miscible Rayleigh–Taylor instability, Phys. Fluids 18 (2006) 045101.
[11] W. Cabot, A. Cook, Reynolds number effects on Rayleigh–Taylor instability with possible implications for type-Ia supernovae, Nat. Phys. 2 (2006) 5621.
[12] C. Canuto, M. Hussaini, A. Quarteroni, T. Zang, Spectral Methods in Fluid Dynamics, Springer-Verlag, Berlin, 1988.
[13] P. Chassaing, R. Antonia, F. Anselmet, L. Joly, S. Sarkar, Variable Density Fluid Turbulence, Fluid Mech. Appl., vol. 69, Kluwer Academic Publishers, Dordrecht, 2002.
[14] A. Chorin, Numerical solution of the Navier–Stokes equations, Math. Comput. 22 (1968) 745–761.
[15] B.-T. Chu, L. Kovásznay, Non-linear interactions in a viscous heat-conducting compressible gas, J. Fluid Mech. 3 (1957) 494–514.
[16] A. Cook, P. Dimotakis, Transition stages of Rayleigh–Taylor instability between miscible fluids, J. Fluid Mech. 443 (2001) 69–99.
[17] A. Cook, W. Cabot, P. Miller, The mixing transition in Rayleigh–Taylor instability, J. Fluid Mech. 511 (2004) 333–362.
[18] R. Duff, F. Harlow, C. Hirt, Effects of diffusion on interface instability between gases, Phys. Fluids 5 (1962) 417.
[19] D. Durran, A physically motivated approach for filtering acoustic waves from the equations governing compressible stratified flow, J. Fluid Mech. 59 (2008) 365–379.
[20] J. Fröhlich, R. Peyret, Calculations of non-Boussinesq convection by a pseudo-spectral method, Comput. Methods Appl. Mech. Eng. 80 (1990) 425–433.
[21] S. Gauthier, A semi-implicit collocation method: application to thermal convection in 2D compressible fluids, Int. J. Numer. Methods Fluids 12 (1991) 985–1002.
[22] S. Gauthier, Compressibility effects in Rayleigh–Taylor flows: influence of the stratification, Phys. Scr. T 155 (2013), 014012-8.
[23] S. Gauthier, B. Le Creurer, F. Abéguilé, C. Boudesocque-Dubois, J.-M. Clarisse, A self-adaptive domain decomposition method with Chebyshev method, Int. J. Pure Appl. Math. 24 (2005) 553–577.
[24] E. George, J. Glimm, Self-similarity of Rayleigh–Taylor mixing rates, Phys. Fluids 17 (2005), 054101-13.
[25] J. Glimm, D. Sharp, T. Kaman, H. Lim, New directions for Rayleigh–Taylor mixing, Philos. Trans. R. Soc. A 371 (2013) 20120183 (17 pp.).
[26] D. Gough, The anelastic approximation for thermal convection, J. Atmos. Sci. 26 (1969) 448–456.
[27] H. Guillard, J.-M. Malé, R. Peyret, Adaptive spectral methods with application to mixing layer computations, J. Comput. Phys. 102 (1992) 114–127.
[28] W. Guo, G. Labrosse, R. Narayanan, The Application of the Chebyshev-Spectral Method in Transport Phenomena, Lect. Notes Appl. Comput. Mech., vol. 68, Springer-Verlag, Berlin, Heidelberg, 2013.
[29] Z. Hammouch, Développement d'une méthode numérique pour les équations de Navier–Stokes en approximation anélastique: application aux instabilités de Rayleigh–Taylor, PhD thesis, Université de Paris-Sud 11, 2012.
[30] Z. Hammouch, G. Labrosse, S. Gauthier, Anelastic Stokes eigenmodes in infinite channel, J. Sci. Comput. 55 (2013) 65–91.
[31] L. Joly, J. Fontane, P. Chassaing, The Rayleigh–Taylor instability of two-dimensional high-density vortices, J. Fluid Mech. 537 (2005) 415–431.
[32] G. Karniadakis, M. Israeli, S. Orszag, High-order splitting methods for the incompressible Navier–Stokes equations, J. Comput. Phys. 97 (1991) 414–443.
[33] L. Kleiser, U. Schumann, Treatment of the incompressibility and boundary conditions in 3-D numerical spectral simulation of plane channel flows, in: E. Hirschel (Ed.), Proc. 3th GAMM Conf. on Numerical Methods in Fluid Mechanics, Vieweg, Braunschweig, 1980, pp. 165–173.
[34] G. Labrosse, Méthodes spectrales: méthodes locales, méthodes globales, problèmes d'Helmholtz et de Stokes, équations de Navier–Stokes, Collection Technosup, Ellipses, Paris, 2011.
[35] G. Labrosse, A. Redondo, The optimal 3-node preconditioner of the d^2/dx^2 Fourier and Chebyshev spectral operators, J. Comput. Phys. 230 (2011) 147–158.
[36] E. Leriche, G. Labrosse, High-order direct Stokes solvers with or without temporal splitting: numerical investigations of their comparative properties, SIAM J. Sci. Comput. 22 (2000) 1386–1410.
[37] D. Livescu, Numerical simulations of two-fluid turbulent mixing at large density ratios and applications to the Rayleigh–Taylor instability, Philos. Trans. R. Soc. A 371 (2003) (2013) 20120185 (23 pp.).
[38] D. Livescu, J. Ristorcelli, Variable-density mixing in buoyancy-driven turbulence, J. Fluid Mech. 605 (2008) 145–180.
[39] D. Livescu, T. Wei, M. Petersen, Direct numerical simulations of Rayleigh–Taylor instability, J. Phys. Conf. Ser. 318 (2011) 082007.
[40] M. Macaraeg, C. Street, Improvements in spectral collocation discretization through a multiple domain technique, Appl. Numer. Math. 2 (1986) 95–108.
[41] R. McLaughlin, H. Zhou, G. Forest, Computational study of a weakly compressible mixing barrier in low Prandtl number, strongly stratified fluids, Phys. Fluids 15 (10) (2003) 2872–2885.
[42] N. Mueschke, O. Schilling, Investigation of Rayleig–Taylor turbulence and mixing using direct numerical simulation with experimentally measured initial conditions. I. Comparison to experimental data, Phys. Fluids 21 (2009) 014106 (19 pp.).
[43] N. Mueschke, O. Schilling, Investigation of Rayleigh–Taylor turbulence and mixing using direct numerical simulation with experimentally measured initial conditions. II. Dynamics of transitional flow and mixing statistics, Phys. Fluids 21 (2009) 014107 (16 pp.).
[44] Y. Ogura, N. Phillips, Scale analysis of deep and shallow convection in the atmosphere, J. Atmos. Sci. 19 (1962) 173–179.
[45] S. Orszag, Spectral methods for problems in complex geometries, J. Comput. Phys. 37 (1980) 70–90.
[46] R. Peyret, Spectral Methods for Incompressible Viscous Flow, Springer, New York, 2002.
[47] F. Renaud, S. Gauthier, A dynamical pseudo-spectral domain decomposition technique: application to viscous compressible flows, J. Comput. Phys. 131 (1997) 89–108.
[48] R. Richtmyer, K. Morton, Difference Methods for Initial-Value Problems, 2nd edition, Wiley-Interscience, 1967.
[49] J. Ristorcelli, T. Clark, Rayleigh–Taylor turbulence: self-similar analysis and direct numerical simulations, J. Fluid Mech. 507 (2004) 213–253.
[50] D. Sandoval, The dynamics of variable-density turbulence, PhD thesis, University of Washington, 1995.
[51] N. Schneider, S. Gauthier, Asymptotic analysis of Rayleigh–Taylor flow for Newtonian miscible fluids, J. Eng. Math. (2015), http://dx.doi.org/10.1007/s10665-014-9765-7.

[52] N. Schneider, S. Gauthier, Visualization of Rayleigh–Taylor flows from Boussinesq approximation to fully compressible Navier–Stokes model, 2015, submitted for publication.
[53] R. Temam, Sur l'approximation de la solution de Navier–Stokes par la méthode des pas fractionnaires. I, II, Arch. Ration. Mech. Anal. 32 (1969) 135–153, 377–385.
[54] N. Vladimirova, M. Chertkov, Self-similarity and universality Rayleigh–Taylor, Boussinesq turbulence, Phys. Fluids 21 (2009) 015102 (9 pp.).
[55] J. Waddell, C. Niederhaus, J. Jacobs, Experimental study of Rayleigh–Taylor instability: low Atwood number liquid systems with single-mode initial perturbations, Phys. Fluids 13 (5) (2001) 1263–1273.
[56] Y.N. Young, H. Tufo, A. Dubey, R. Rosner, On the miscible Rayleigh–Taylor instability: two and three dimensions, J. Fluid Mech. 447 (2001) 377–408.
[57] D. Youngs, The density ratio dependence of self-similar Rayleigh–Taylor mixing, Philos. Trans. R. Soc. A 371 (2013) 20120173 (15 pp.).
[58] X. Zhang, D. Tan, Direct numerical simulation of the Rayleigh–Taylor, with the spectral element method, Chin. Phys. Lett. 26 (8) (2009) 084703 (4 pp.).
[59] M. Zingale, S. Woosley, C. Rendleman, M. Day, J. Bell, Three-dimensional numerical simulations of Rayleigh–Taylor unstable flames in Type Ia supernovae, Astrophys. J. 632 (2005) 1021–1034.